UNIVERSITY OF COPENHAGEN
FACULTY OF SCIENCE

MSc in Climate Change

Convecting the dots

Processes of open-ocean deep convection in Veros and their role in setting the properties of the Atlantic Meridional Overturning Circulation

Simon Storvig Winther

Supervised by Markus Jochum

May 2024

Simon Storvig Winther
Convecting the dots
MSc in Climate Change, May 2024
Supervisor: Markus Jochum

University of Copenhagen
Faculty of Science
Niels Bohr Institute
Blegdamsvej 17
2200 Copenhagen N

Acknowledgements

I wish to thank my supervisor, prof. Markus Jochum, for guidance throughout the process. I would also like to thank Roman Nuterman for crucial help with techonological difficulties, and the rest of TeamOcean, for sharing their knowledge and company. Finally, I would like to thank Edel Malene Farstad for proofreading.

Abstract

Processes of deep water formation in the North Atlantic play an important role in setting the strength and structure of the North Altantic deep water (NADW), and may be linked to possible transient behaviour of the Atlantic meridional overturning circulation (AMOC). This thesis seeks to investigate how local-scale details of open-ocean deep convection may impact large-scale adjustments of the AMOC, using an idealized sector model of the Atlantic Ocean in Veros, an ocean-only GCM. Veros is found to be able to reproduce the local processes of open-ocean convection to a satisfactory degree. It is found that convection near vertical boundaries differs from open-ocean convection locally and at short-timescales, but that global differences are negligible over long timescales. Implementing a meso-scale eddy mixing closure with diffusivities determined by a prognostic eddy-kinetic energy (EKE) closure, as opposed to constant eddy diffusivities, does not result in any important differences to the large-scale adjustment. Initial AMOC adjustment is found to be communicated by boundary waves propagating from the region of open-ocean convection first along the northern boundary and then southwards along the western boundary. Regarding the upwelling branch of the AMOC, it is found that with coarse resolution, the model is dominated by upwelling in the western boundary current (WBC). If resolution is increased, the dominance of the WBC upwelling relative to the interior is reduced.

Contents

Introduction

1

The Atlantic meridional overturning circulation (AMOC) plays a central role in the Earth's climate system. The AMOC is characterized by the northward flow of warm and salty water in the upper kilometer of the Atlantic and the southward flow of colder and fresher North Atlantic deep water (NADW) at depths between approximately 1 and 3 km. The system is responsible for a net northward transport of heat across both hemispheres of the Atlantic basin (Johnson *et al.*, 2019; Kuhlbrodt *et al.*, 2007). Accurately representing the various processes involved in the overturning circulation is therefore a crucial task for climate models. One aspect of importance is the role of surface buoyancy fluxes in the form of heat and freshwater in deepwater formation (DWF) in the North Atlantic, and associated contribution to setting the shape and strength of the NADW cell. This is of particular interest due to the predictions that changing surface buoyancy fluxes in the form of heat and freshwater may be linked to transient behaviour of the AMOC. Yet, processes of NADW are not represented to a satisfactory degree in coupled climate models, causing variation in predictions for future AMOC changes (Kuhlbrodt *et al.*, 2007).

This thesis focuses on processes of open-ocean convection and their role in NADW formation. While the ocean in general is stably stratified with a strong vertical density gradient in the thermocline effectively insulating the deep ocean from changes in surface properties, there are certain regions where the stratification is weaker. In these regions, given the right conditions, a strong surface buoyancy loss to the atmosphere may lead to intense convective events where surface waters are vigorously mixed to great depths. Through such deep convective events, variations in surface properties may reach the abyss, contributing to setting and maintaining its properties (Marshall and Schott, 1999). Sites of open-ocean deep convection will be referred to as mixed patches or convective patches throughout this thesis.

Although much research exists on details of the open-ocean convective process (see for example Klinger *et al.* (1996), Kovalevsky *et al.* (2020), Maxworthy and Narimousa (1994), Send and Marshall (1995), Sohail *et al.* (2020), and Visbeck *et al.* (1996)), as well as on southward propagation of buoyancy

anomalies from the North Atlantic and resulting AMOC variability (see for example Buckley *et al.* (2023), Buckley *et al.* (2012), Getzlaff *et al.* (2005), and Li *et al.* (2021)), a thorough understanding of how the small scale processes of convection and large scale circulation are connected is still lacking (Marotzke, 2023). In this thesis I seek to investigate how details of open-ocean convection at the local scale may impact the large-scale adjustment of the AMOC.

By enforcing a strong surface buoyancy flux over spatially constrained regions at high latitudes, I will first explore the short-term local response, and compare this qualitatively and quantitatively to observational and theoretical descriptions of open-ocean convection (see section 2.2 for details). Next, I will look into the long-term response in density-space, in an attempt to better understand the role of diapycnal mixing in setting the properties of the NADW and the adjustment of the meridional overturning circulation (MOC) (see section 2.4 for details). I will then move on to investigating the large-scale and long-term adjustment of the strength and structure of the MOC in depth-space, before attempting to connect the local and global scales by examining signal propagation from the region of localized forcing and towards the equator (see section 2.5). Finally as a slight detour, I will briefly consider aspects of the upwelling branch of the circulation, as this is crucial in understanding the full picture of the AMOC, even if somewhat outside the scope of this thesis (see section 2.6).

Throughout, I will explore how variation in lateral viscosity, numerical implementation of meso-scale eddy mixing, adjacency of the forcing region to vertical boundaries, and horizontal resolution impact the processes at hand. All experiments will be conducted in an idealized sector representing the Atlantic Ocean using Veros, a primitive equation finite difference ocean model (Häfner *et al.*, 2018). My approach is predominantly exploratory. However, I will attempt to address four specific questions:

1. Vorticity constraints imply that mean vertical transport in open-ocean convection must be negligible, while presence of lateral boundaries are expected to break the rotational constraints allowing for net downwelling in the patch (see sections 2.2.3 & 2.2.4). **Does surface-forced convection adjacent to a vertical boundary result in significantly different large-scale AMOC adjustment than convection in open ocean?**

2. Baroclinic eddy transport between the mixed patch and its surroundings play an important role in setting the properties of the patch, and the

parameterization of meso-scale eddy transport has been suggested to be a key compromising factor in coarse-resolution models (see section 2.2.6). **How will the local processes of open-ocean convection and the subsequent large-scale adjustment differ if meso-scale eddy diffusivities are determined prognostically with variation in space and time, as opposed to being given by pre-set constant parameters?**

3. Whether buoyancy anomalies propagate from high latitudes towards the equator by boundary waves or advection remains an open question (see section 2.5). **How do signals propagate from the mixed patch and to the equator in the experiments at hand, and how does the propagation timescales correspond to timescales of the MOC adjustment?**

4. Coarse-resolution models may generate too large diapycnal transport at vertical boundaries, leading to excessive upwelling in the western boundary current (WBC) (see section 2.6). **How is upwelling distributed between the WBC and the interior in the model at hand, and how is this affected by the horizontal resolution?**

The thesis is structured as follows: In Chapter 2, I present background in terms of fundamental geophysical concepts, a review of theory and findings on open-ocean deep convection, definitions and theoretical frameworks used in the analysis, and brief overviews on signal propagation and upwelling in the WBC. In Chapter 3, an introduction to Veros and the specific model set-up is given, as well as descriptions of the conducted experiments. In Chapter 4, the experimental results are presented and analysed. Chapter 5 attempts to summarize the findings and put them into context, answer the four main questions outlined above and present suggestions for further research.

Background

2

2.1 Fundamentals

2.1.1 The simple Boussinesq equations

Before delving into the details of open-ocean convection, some necessary fundamental geophysical concepts will be outlined. Considerations and notation in this section will largely follow Vallis (2017). The momentum equation describes how the momentum of a fluid parcel acts in response to internal and imposed forces. For an incompressible fluid with uniform viscosity on a rotating planet, the equation may be written on vector form as

$$\frac{\partial \boldsymbol{v}}{\partial t} + (\boldsymbol{v} \cdot \boldsymbol{\nabla})\boldsymbol{v} + 2\boldsymbol{\Omega} \times \boldsymbol{v} = -\frac{1}{\rho}\nabla p + \nu \nabla^2 \boldsymbol{v} + g\hat{\boldsymbol{z}} + \boldsymbol{F}_b. \tag{2.1}$$

Here, $\boldsymbol{v}$ is the three-dimensional velocity-vector, $\boldsymbol{\Omega}$ the angular velocity of the rotating frame, ρ the density, p the pressure, $\nu \equiv \mu/\rho$ the kinematic viscosity (with μ the viscosity), and g the gravitational acceleration. Respectively, the individual terms represent acceleration, advection, the Coriolis force, pressure-gradient force, viscous effects, gravitational force, and any remaining external body forces $\boldsymbol{F}_b$.

First, we will apply the Beta-plane approximation, so that the Coriolis-force is given by $\boldsymbol{f} \times \boldsymbol{v}$, where $\boldsymbol{f} = (f_0 + \beta y)\hat{\boldsymbol{z}}$ is the Coriolis parameter, with $\beta = \partial f/\partial y$ and $f_0 = 2\Omega \sin \phi_0$, ϕ_0 being a given reference latitude. This approximation simplifies the equations involving the Coriolis-effect, while still capturing essential effects of sphericity (Vallis, 2017).

Then, an appropriate next step is to apply the Boussinesq approximation to an inviscid fluid. Assume that variations $\delta\rho(x, y, z, t)$ in density are sufficiently small around some much larger constant reference density ρ_0. Next, assume the reference density is in hydrostatic balance with a reference pressure $p_0(z)$, and that the deviation in density is in hydrostatic balance with the pressure deviation $\delta p(x, y, z, t)$, giving

$$\frac{\partial p_0}{\partial z} = -g\rho_0, \quad \frac{\partial \delta p}{\partial z} = -g\delta\rho. \tag{2.2}$$

As with density, it is assumed that $p_0(z) \gg |\delta p|$. In this case, density variation in (2.1) may be ignored in all terms on the left hand side, while the gradient of p_0 and the gravitational force associated with ρ_0 cancel as given by the hydrostatic balance. The simple Boussinesq equations can then be formulated as

$$\frac{D\boldsymbol{v}}{Dt} + \boldsymbol{f} \times \boldsymbol{v} = -\frac{1}{\rho_0}\nabla \delta p + b\hat{\boldsymbol{z}}, \qquad \text{(momentum equations)} \tag{2.3}$$

$$\nabla \cdot \boldsymbol{v} = 0, \qquad \text{(mass conservation)} \tag{2.4}$$

$$\frac{Db}{Dt} = \dot{b}, \qquad \text{(buoyancy equation)}. \tag{2.5}$$

Here, we have introduced the buoyancy,

$$b = -g\frac{\delta \rho}{\rho_0}, \tag{2.6}$$

which describes the force acting on a water parcel due to a density anomaly with regards to its surroundings. This will prove to be an important variable when dealing with open-ocean convection. To close the set of equations, we introduce the mass conservation equation (2.4), where we assume the fluid is incompressible, as well as the buoyancy equation (2.5), where $\dot{b}$ is the buoyancy forcing or rate of buoyancy input, and $\frac{D}{Dt} = \frac{\partial}{\partial t} + \boldsymbol{v} \cdot \nabla$ is the material derivative.

Closing the set of equations with (2.5) assumes that the fluid is incrompressible, and ignores the complicated and nonlinear ways that the density of seawater depends on potential temperature θ and salinity S. Inaccuracies stemming from the first assumption is resolved by inserting the potential buoyancy b_σ in place of b, while closing the set of equation with a more accurate equation of state equation of state $b = b(\theta, S, p)$ would require treating salinity- and temperature forcings individually.

In a vertically stratified ocean, it is reasonable to assume that the processes causing the vertical variation in $\delta\rho(x, y, z, t)$ behave differently than in horizontal directions. It is therefore useful to separate out the variation in buoyancy associated with the stratification, writing

$$b = \tilde{b}(z) + b'(x, y, z, t). \tag{2.7}$$

Then, the vertical advection of the reference stratification can be separated out in (2.5), and the equation may be reformulated as

$$\frac{Db'}{Dt} + N^2 w = \dot{b}, \tag{2.8}$$

where $N^2 = \partial\tilde{b}/\partial z$ is a measure of the stratification, and its square-root the buoyancy frequency.

2.1.2 Geostrophic balance and thermal wind

Considering now the horizontal terms in the momentum equation, further approximations can be made by comparing the magnitudes of the nonlinear advective terms and the Coriolis terms, their ratio given by the Rossby number $Ro \equiv U/fL$. Here, U is the approximate horizontal velocity and L is the typical length scale of horizontal velocity variation. It is assumed that the aspect ratio of the ocean is small, so that contributions from vertical advection can be neglected. If the Rossby number is small, which is an appropriate assumption in much of the ocean (Vallis, 2017), the Coriolis term will dominate the advective term. In steady state, the pressure gradient is the only term that can balance the rotational term, giving rise to the geostrophic balance. With the Boussinesq approximation, the balance may be written in Cartesian component form as

$$-fv_g \equiv -\frac{1}{\rho_0}\frac{\partial \delta p}{\partial x}, \quad fu_g \equiv -\frac{1}{\rho_0}\frac{\partial \delta p}{\partial y}, \tag{2.9}$$

where u_g and v_g are the geostrophic velocities. With hydrostatic balance assumed, the second relation in (2.2) can be combined with (2.6) and inserted into the geostrophic balance, giving

$$-f\frac{\partial v_g}{\partial z} = -\frac{\partial b}{\partial x} \tag{2.10}$$

$$f\frac{\partial u_g}{\partial z} = -\frac{\partial b}{\partial y}. \tag{2.11}$$

This is the thermal wind balance with the Boussinesq approximation. As will be shown in 2.2.5, the thermal wind balance plays a key role in the processes governing open-ocean convection.

2.1.3 Vorticity

Returning to the horizontal momentum equation in the case of a small Rossby number as given in (2.9), but this time without assuming steady state,

$$\frac{\partial u}{\partial t} - fv \equiv -\frac{1}{\rho_0}\frac{\partial \delta p}{\partial x}, \tag{2.12}$$

$$\frac{\partial v}{\partial t} + fu \equiv -\frac{1}{\rho_0}\frac{\partial \delta p}{\partial y}. \tag{2.13}$$

Taking the curl of the two equations above, we obtain the time-dependent linear vorticity balance,

$$\frac{\partial \zeta}{\partial t} + \beta v - f\frac{\partial w}{\partial z} = 0, \tag{2.14}$$

The first term is the time-derivative of the relative vorticity,

$$\boldsymbol{\zeta} = \nabla_H \times \boldsymbol{u} = v_x - u_y, \tag{2.15}$$

defined as the vertical component of the vorticity $\boldsymbol{\omega} = \nabla \times \boldsymbol{v}$. The second term is the advection of planetary vorticity, where $\beta = \partial f/\partial y$ as given by the Beta-plane approximation has been used, and the third term is found using (2.4). The pressure-gradient terms on the right hand side cancel when cross-differentiating.

The relation given above indicates that vortex stretching or squeezing as described by the third term must be associated with either meridional transport or a change in relative vorticity. As will be shown in 2.2.3, this implies an important constraint to open-ocean convection.

2.2 Open-ocean deep convection

2.2.1 Formation and phases of open-ocean deep convection

Open-ocean convective events may be described in three phases: *preconditioning*, *deep convection*, and *lateral exchange and spreading* (Marshall and Schott, 1999). The preconditioning-phase is characterized by a destabilizing surface buoyancy-flux caused by changes to circulation patterns and surface conditions such as temperature, ice-formation or winds. This leads to large-scale doming of the surface isopycnals and a weakening of the vertical stratification in the upper ocean (Sohail *et al.*, 2020). In the case of sustained or strengthened surface buoyancy forcing, in the North-Atlantic typically by surface cooling in the winter, the remaining stratification in the upper ocean is eroded away by

the buoyancy loss to the atmosphere (Marshall and Schott, 1999). Subsequent cooling then initiates the deep convection. This phase is characterized by rapid vertical buoyancy transport and vigorous mixing of water properties between the surface and the deep ocean. While the preconditioning can happen on scales up to a few hundred kilometers, the deep convection itself is characterized by turbulent convective plumes with horizontal scales smaller than 1 km. The plumes are distributed across the preconditioned convective site and form a patch of deep mixing, typically with horizontal scales ranging from ~ 10 km to ~ 100 km in diameter and vertical scales up to 2000 m (Marshall and Schott, 1999; Sohail *et al.*, 2020).

While the mixed patches are regions of vertical buoyancy transport, the net vertical transport of water masses is neglible within the region due to geostrophic constraints, as will be described in more detail in section 2.2.3. As a consequence of the vertical buoyancy transport within the patch, a strong lateral density gradient between the mixed patch and the surrounding water arises, leading to a horizontal geostrophic current around the edge of the patch caused by the thermal wind balance. This current will be unstable to baroclinic instability if the radius of the mixed patch is larger than the Rossby deformation radius (Sohail *et al.*, 2020). In the North-Atlantic, the first mode of the local Rossby deformation radius is on the order of 10 km (Chelton *et al.*, 1998). The lateral exchange and spreading-phase is characterized by the unstable geostrophic current breaking up into baroclinic eddies on the scale of 10 km, laterally exchanging fluid between the mixed patch and its surroundings. During this phase, the vertical buoyancy exchange by eddies dominate the vertical buoyancy transport by convection and halt further deepening of the convective layer. On timescales ranging from weeks to a few months, the fluid mixed by the deep convection will disperse, driven by gravity and rotation, and spread out to its neutrally buoyant level while the mixed patch will disintegrate and restratify. The lateral exchange and spreading-phase can often occur concurrently with the deep convection-phase (Marshall and Schott, 1999; Sohail *et al.*, 2020).

2.2.2 Plume dynamics: scaling relations and the natural Rossby number

It is useful to describe a convective event in terms of scaling relations and non-dimensional parameters that capture central properties of the processes involved. First, considering the dynamics on plume-scales, key scaling rela-

tions can be developed following the approach of Jones and Marshall (1993). Consider a buoyancy loss

$$\mathscr{B}_0 = \frac{g}{\rho_0}\left(\frac{\alpha}{C_p}Q_H - \rho_0\beta Q_S\right) \tag{2.16}$$

at the surface of a neutral fluid of depth H. Here, $\rho_0 = 1024$ kg/m^3 is the reference density, $C_p = 3986$ Jkg^{-1}K^{-1} is the specific heat capacity of water, $\alpha = 1.67 \times 10^{-4}$ K^{-1} and $\beta = 0.78 \times 10^{-3}(g/kg)^{-1}$ are the thermal and haline contraction coefficients respectively, and Q_H [Wm^{-2}] and Q_S [kgm^{-2}s^{-1}g/kg] the net heat and salinity flux into the ocean respectively. In a stratified ocean, H can be assumed to be the mixed layer depth (MLD), above which $N^2 \approx 0$. In the initial stages, where time t is much smaller than f^{-1}, so that the effects of the earth's rotation are still negligible, and assuming that the scale of the individual plumes is still much smaller than H, then the controlling parameter must be $\mathscr{B}_0$. By dimensional arguments, with units m^2/s^3 for the buoyancy flux $\mathscr{B}_0$, and while considering the development in time t, the following scaling relations can be formed:

$$\begin{aligned} l &\sim (\mathscr{B}_0 t^3)^{1/2}, \\ u &\sim w \sim (\mathscr{B}_0 t)^{1/2} \end{aligned} \tag{2.17}$$

where l is the characteristic length scale of the plumes, u and w are the scales of velocities in horizontal and vertical directions.

As the process develops in time, two limiting cases should be considered, where the plume scales are either constrained by the depth of the ocean or by the earth's rotation. In the first case where H is the constraining factor, the scaling relations are independent of rotation:

$$\begin{aligned} l &\sim l_{norot} \sim H, \\ u &\sim u_{norot} \sim (\mathscr{B}_0 H)^{1/3}, \end{aligned} \tag{2.18}$$

where the subscript $norot$ denotes the absence of influence from rotation (Jones and Marshall, 1993).

In the other constraining case, the ocean is sufficiently deep so that the descending convective layer comes under geostrophic control before the plumes

feel the ocean bottom. This happens as t approaches f^{-1}, so that t in (2.17) can be replaces by f^{-1}, which gives scaling relations independent of H:

$$\begin{aligned} l &\sim l_{rot} \sim (\mathscr{B}_0/f^3)^{1/2}, \\ u &\sim u_{rot} \sim (\mathscr{B}_0/f)^{1/2}, \end{aligned} \tag{2.19}$$

where the subscript rot denotes the scales where the plumes come under rotational control, marking the transition from three-dimensional, thermally driven turbulence to quasi-two-dimensional, rotationally dominated motion (Jones and Marshall, 1993).

From the ratio between the length scales of the rotationally constrained case and the depth-constrained case, a useful nondimensional parameter can be defined, the natural Rossby number, Ro^*:

$$Ro^* = \frac{l_{rot}}{H} = \left(\frac{\mathscr{B}_0}{f^3 H^2} \right)^{1/2}. \tag{2.20}$$

This parameter may be seen as a measure of the importance of rotation on the convective process (Jones and Marshall, 1993). Typical values of Ro^* for open-ocean deep convection range from 0.01 to 1 (Marshall and Schott, 1999). If the square of the natural Rossby number is taken, it can also be interpreted as a nondimensional measure of the intensity of the surface buoyancy forcing in relation to depth and rotation (Marshall *et al.*, 1994).

Send and Marshall (1995) find another useful interpretation of the natural Rossby number. In order to determine the timescales of vertical mixing, they argue that the time t_{mix} it takes for a plume to reach H scales as

$$t_{mix} \sim \frac{H}{w_{plume}} \sim H \mathscr{B}_0^{-1/2} f^{1/2}, \tag{2.21}$$

with w_{plume} being the vertical velocity of the plume, which in the rotationally governed regime is assumed to scale as $w_{plume} \sim u_{rot} \sim (\mathscr{B}_0/f)^{1/2}$, as described above. The ratio of the mixing timescale to the rotational adjustment timescale f^{-1} gives

$$\frac{f^{-1}}{t_{mix}} \sim H^{-1} \mathscr{B}_0^{1/2} f^{-3/2} = Ro^*, \tag{2.22}$$

showing how Ro^* can be interpreted as a measure of how long it takes to mix water to the bottom of the convective region (Send and Marshall, 1995).

2.2.3 Plumes as mixing agents

When dealing with the role of open-ocean convection in deep-water formation, it may be tempting to think of the mixed patches as vertical conduits where newly formed dense water masses sink down to the depths of similar densities. In spatially localized regions of deep convection at high latitudes, rotational constraints on vertical water mass transport within the convective patch suggest that this is not the case (Spall and Pickart, 2001; Send and Marshall, 1995; Marotzke, 2023). Following the argument of Send and Marshall (1995), start from the linear vorticity balance (2.14) for the mixed patch,

$$\frac{\partial \overline{\zeta}}{\partial t} = f \frac{\partial \overline{w}}{\partial z}, \tag{2.23}$$

where the overbar indicates an average over the convective patch, f is the coriolis force, w the vertical velocity, and ζ the relative vorticity. It is assumed that the meridional velocity averaged over the patch is zero. If the convective patches act like conduits, the convergence of water masses at the surface and the corresponding changes to the vertical motion within the patch would induce horizontal rim-currents around the edge of the convective region. A mean relative vorticity $\overline{\zeta}$ within a patch of radius R gives a rim-current of magnitude

$$u_{rim} = \frac{R\overline{\zeta}}{2}, \tag{2.24}$$

as given by (2.15). Integrating (2.23) and inserting it into (2.24) then gives the scaling

$$u_{rim} \sim \frac{Rf\overline{w}}{H} t, \tag{2.25}$$

where H is the depth of the convective plume. With typical scales $R \sim 10 - 100$ km, $f \sim 10^{-4}$ s^{-1}, $H \sim 1000$ m and t on the order of a few days, it is evident that any non-neglible values for $\overline{w}$ would lead to unrealistically large u_{rim}. This indicates that vertical motion in the plumes must be compensated by upwelling inbetween the plumes, resulting in a net $\overline{w} \sim 0$ inside the mixed patch. The alternative view of open-ocean convection, where the mixed patches act as regions of vigorous mixing rather than conduits of vertical water mass transport, must therefore be the case (Send and Marshall, 1995).

2.2.4 Convection near a boundary

As discussed in section above, downwelling in regions of open-ocean convection must be neglible due to rotational constraints. This is not the case if the

convection happens adjacent to a vertical or steep boundary, as argued by Spall and Pickart (2001). In this case, the boundary can support a lateral pressure gradient breaking the geostrophic constraints, as the vortex stretching associated with the downwelling is balanced by lateral diffusion of vorticity into the boundary (Spall and Pickart, 2001; Johnson *et al.*, 2019). This means that the unrealistically strong rim-currents are not induced, and downwelling near the boundary can occur.

2.2.5 Mixed patch dynamics: equilibrium depth and timescales

The relations in 2.2.3 describe the development of plumes in an already homogeneous fluid where $N^2 \approx 0$, such as within the mixed layer. However, in order to describe the process of mixed-layer deepening during the *deep convection*-phase, as well as the processes of the *lateral exchange and spreading*-phase, one must also consider convection in a stratified ocean. By evaluating a quasi-steady-state balance between the processes of vertical buoyancy transport characterizing the deep convection, and lateral buoyancy transport by eddies characterizing the lateral spreading, Visbeck *et al.* (1996) derives scaling relations for the equilibrium depth and timescale of the mixed patch in an ocean of uniform stratification N. The relations, described below, has been found to align well with results given by a fine-scale, turbulence resolving non-hydrostatic model by Sohail *et al.* (2020).

Consider again a surface buoyancy loss $\mathscr{B}_0$ over a convective mixed patch of surface area A, assumed to be shaped as a cylinder of depth h. If the depth of the mixed patch is taken to be where the vertical buoyancy flux through the bottom of the cylinder is zero, and the lateral buoyancy flux into the cylinder by baroclinic eddies is given by the mean product of the eddy velocity v' and the buoyancy anomaly b', then at steady state the total buoyancy-budget of the patch balances as

$$\int\int \mathscr{B}_0 dA = \int_h^0 \oint \overline{v'b'} dl dz. \tag{2.26}$$

Integrating over the depth and area of the mixed patch then gives

$$\overline{v'b'} = \frac{\mathscr{B}_0 r}{2h}, \tag{2.27}$$

as derived in Visbeck *et al.* (1996). The eddy velocity can be assumed to scale with the velocity u_{rim} of the geostrophic rim-current (Sohail *et al.*, 2020;

Visbeck *et al.*, 1996), which can be related to the buoyancy anomaly by the thermal wind balance as given in (2.11),

$$v' \sim u_{rim} \sim \frac{\Delta b \Delta z}{\Delta y f} \sim \frac{b'}{N}. \tag{2.28}$$

In the final relation, the vertical length scale Δz is assumed to scale with the depth h of the mixed path, and the horizontal scale Δy is assumed to scale as the mixed layer Rossby deformation radius $L_d = Nh/f$ at steady state (Sohail *et al.*, 2020). Assuming continuous density at the base of the mixed patch, the lateral buoyancy anomaly scales as $b' \sim N^2 h$ (Visbeck *et al.*, 1996). Combining this with equations (2.26) and (2.28) then gives the depth at which the deepening of the mixed layer is arrested by the lateral eddy buoyancy flux as derived by Visbeck *et al.* (1996),

$$h_{final} = \gamma \frac{(\mathscr{B}_0 r)^{1/3}}{N}. \tag{2.29}$$

Here, γ is an empirical constant of proportionality that depends on the efficiency of baroclinic eddy transfer. Visbeck *et al.* (1996) find that $\gamma = 3.9 \pm 0.9$, while Sohail *et al.* (2020) find $\gamma = 1.76$.

In the initial stages of the convection, it can be assumed that the deepening of the mixed patch will follow the classical result of nonpenetrative deepening of a mixed layer exposed to a surface buoyancy loss (Visbeck *et al.*, 1996). Returning to the buoyancy equation for a stratified fluid as given by (2.8), we can derive the classical result under the assumptions that the convective layer is vertically homogeneous, that the vertical buoyancy flux through the base of the mixed layer can be neglected, and that horizontal advection can be neglected, following Visbeck *et al.* (1996). In this case, the only remaining term on the left hand side in (2.8) is the advection of the mean stratification. The buoyancy forcing on the right hand side is given by $\dot{b} = \partial \mathscr{B} / \partial z$, where $\mathscr{B}$ is the buoyancy flux. Integrating both sides over depth h of the mixed patch, and with the assumption of zero buoyancy flux through the base, we obtain

$$N^2 \frac{\partial h}{\partial t} = \frac{\mathscr{B}_0}{h}, \tag{2.30}$$

where $\mathscr{B}_0$ is the surface buoyancy flux. From the equation above, the classical result as given in Visbeck *et al.* (1996) is obtained,

$$h(t) = \frac{(2\mathscr{B}_0 t)^{1/2}}{N}. \tag{2.31}$$

Combining equations (2.29) and (2.31), the result of Visbeck *et al.* (1996) for the equilibrium timescale of the mixed patch can be obtained,

$$t_{final} = \beta \left(\frac{r^2}{\mathscr{B}_0} \right)^{1/3}. \tag{2.32}$$

The constant of proportionality, β, is expected to be bounded in the lower end by $\gamma^2/2$ (Visbeck *et al.*, 1996). Visbeck *et al.* (1996) find $\beta = 12 \pm 3$.

2.2.6 Parameterization of deep convection in ocean models

Key processes in open-ocean deep convection happen on scales smaller than typical horizontal resolutions in climate models. Models with horizontal resolution ~ 100 km barely resolve typical mixed patch-scales, and certainly not the baroclinic eddy scale or the convective plume-scale. Higher resolution eddy-permitting models with grid scales on the order ~ 10 km are, as their name indicates, expected to better capture baroclinic eddy-processes even if the resolution is still too coarse to fully resolve them. These models are still in need of a parameterization of the convective plume-scale (Marshall and Schott, 1999).

A common way of representing convective processes in general circulation models is by convective adjustment- or enhanced diffusivity-schemes. Different implementations exist, but in essence all such schemes remove static instabilities in a water column (due to denser fluid being placed over lighter) by vertical mixing within the column. The mixing may be instantaneous or with a finite adjustment timescale using enhanced vertical diffusion, and the mixing may occur between adjacent layers only, or throughout the entire unstable section of the column (Marshall and Schott, 1999). Regardless, the various implementations all ensure that the mixed patches are regions of efficient mixing rather than vertical mass exchange, and thus capture a key aspect of convective plumes as argued in 2.2.5.

Two issues should be addressed with regards to convective adjustment as a parameterization of convective plumes. First is the mixing timescale, t_{mix}, which

is expected to scale according to (2.22). Observed values for H and w_{plume} suggest a mixing timescale of 12 hours and longer (Marshall and Schott, 1999). Although this means that it is not entirely accurate to assume that the mixing happens instantaneously, Marshall and Schott (1999) argue that the timescale is short enough to be considered essentially instantaneous when large-scale flow is concerned. Alternatively, in an enhanced diffusivity-scheme, the vertical diffusivity may be adjusted according to the scaling in (2.22) (Marshall and Schott, 1999). The next issue is that convective adjustment and enhanced diffusivity necessarily treat the mixed patch as homogeneous on gridsize scales, not capturing the heterogeneity of descending small-scale plumes with compensating upwelling in between, as well as neglecting pre-existing variations in stratification or variations in the forcing. While various implementation have been suggested to work around this issue (see for example Ilıcak *et al.* (2014) for their "patchy convection"-framework), it remains a limitation to be aware of in coarse-resolution models.

As argued in 2.2.5, baroclinic eddies play an important role in the water mass transformation and in setting the properties of the mixed patch. The parameterization of the geostrophic eddy-scale is therefore central in coarse models. In fact, Marshall and Schott (1999) identify parameterizations of processes involved in the *lateral exchange and spreading*-phase as likely to be the largest compromising factor in representing water mass transformation in large-scale models. Based on comparison between parameterized and explicit models, they argue for a Transformed Eulerian Mean-framework where the spreading by geostrophic eddies is represented as an advective process with eddy-induced velocities, such as the parameterization put forward in Gent and Mcwilliams (1990). To determine the magnitude of the eddy-induced velocities of the transport, Marshall and Schott (1999) emphasize the importance of capturing the three-dimensional structure of the eddy-induced velocities, with spatially varying transfer coefficients. They argue for closures that are based on the transfer theory by Green (1970) and Stone (1972) in order to achieve this.

2.3 Defining the AMOC in depth- and density-space

In order to quantify the strength of the complex, three-dimensional global overturning circulation system, it is useful to consider the circulation in the meridional-vertical plane. Defining the MOC as the zonally integrated merid-

ional volume transport, the three-dimensional circulation may be collapsed into a two-dimensional streamfunction. In depth-coordinates z, this is given by

$$\Psi(\phi, z, t) = \int_{z_b}^{z} \int_{x_w}^{x_e} v \mathrm{d}x \mathrm{d}z, \tag{2.33}$$

where v is the meridional velocity, z_b is the ocean depth, and x_w and x_e are the western and eastern boundaries, respectively (Buckley *et al.*, 2023).

In addition to defining the AMOC in depth-coordinates, it is also possible to define the overturning stream function density-space,

$$\Psi(\phi, \sigma, t) = \int_{\sigma_b}^{\sigma} \int_{x_w}^{x_e} v \mathrm{d}x \mathrm{d}\sigma, \tag{2.34}$$

where σ is the potential density and σ_b the maximum density found at the ocean bottom (Buckley *et al.*, 2023). The benefits of considering the AMOC in density-space are clear. Ocean currents flow along isopycnal surfaces, and in regions of sloping isopycnals such as the subpolar North Atlantic, the MOC defined in depth-space gives an inaccurate view of the circulation (Buckley *et al.*, 2023). Furthermore, when considering processes of convection, downwelling in depth- and density-space are fundamentally different (Brüggemann and Katsman, 2019). Open-ocean convective patches are regions of downwelling in density space, but with neglible downwelling in depth-space, as described in 2.2.3.

2.4 Overturning and diapycnal water mass transformation: the Walin framework

Defining the overturning in density space (2.34) makes it possible to connect the overturning to diapycnal water mass transformation through the Walin-framework (Walin, 1982). This is beneficial as it gives insight into how water transformed by surface buoyancy fluxes is modified by diapycnal mixing (Buckley *et al.*, 2023).

Following the approach of Buckley *et al.* (2023) and Xu *et al.* (2018), when considering an enclosed geographical domain between latitudes ϕ_1 and ϕ_2, the volume and buoyancy-bugdet of the region is given by

$$\begin{aligned} F(\phi_1 < \phi < \phi_2, \sigma) + G_D(\phi_1 < \phi < \phi_2, \sigma) = \\ \frac{\partial V(\phi_1 < \phi < \phi_2, \sigma)}{\partial t} + \Psi(\phi_1, \sigma) - \Psi(\phi_2, \sigma), \end{aligned} \tag{2.35}$$

where σ is the potential density of the isopycnal, $F(\phi_1 < \phi < \phi_2, \sigma)$ is the diapycnal volume flux due to air-sea buoyancy fluxes, referred to as the surface water mass transformation, G_D the diapycnal volume flux due to mixing, referred to as the mixing water mass transformation, $V(\phi_1 < \phi < \phi_2, \sigma)$ the volume of fluid denser than the isopycnal layer, and $\Psi(\phi_{1,2}, \sigma)$ the overturning in density space in and out of the domain. The surface water mass transformation F is given by

$$F(\phi_1 < \phi < \phi_2, \sigma) = \frac{1}{\Delta\sigma} \int \int_{\phi_1 < \phi < \phi_2} D\delta(\Delta\sigma) \mathrm{d}x\mathrm{d}y, \tag{2.36}$$

where $\delta(\Delta\sigma)$ is a boxcar function evaluated to 1 when the surface density is within the range $\sigma \pm \Delta\sigma/2$ and zero otherwise, and D is the local rate of surface-forced water mass transformation,

$$D = \alpha C_p^{-1} Q_H - \beta Q_S. \tag{2.37}$$

Here, all parameters are as given in (2.16) (Buckley *et al.*, 2023; Xu *et al.*, 2018). The diapycnal volume flux G_D is assumed to be given by the residual of the other terms, thus closing the budget. G_D will therefore include contributions from all forms of mixing, as well contributions from noise.

2.5 Signal propagation

If the strength and structure of the AMOC is to adjust to a change in high latitude buouancy forcing and deep water formation, there must be some sort of signal propagation of the high latitude buoyancy anomalies to lower latitudes. The exact nature of this signal propagation remains an unsettled question, where the problem in essence is whether the signal is transmitted by advection in the deep WBC, or by boundary waves along the western boundary (Marotzke, 2023; Buckley and Marshall, 2016). The situation is further complicated by the existence of internal pathways and latitude-dependent modes of signal propagation (see for example Buckley and Marshall (2016) and Zhang (2010)).

Theories that point to boundary waves as the mode of signal transmission typically build on the classical theory for AMOC spin-up put forward by Kawase (1987), where subpolar buoyancy anomalies on the western boundary excite Kelvin waves that rapidly propagate southwards to the equator, then eastwards along the equator, before they split up at the eastern boundary and propagate

polewards in both directions with Rossby waves originating on the eastern boundary radiating westwards through the basin (Buckley and Marshall, 2016; Marotzke, 2023). If the Kelvin waves propagate at 1 m/s, a typical speed of the first baroclinic mode, they would reach the tropics from subpolar latitudes within timescales on the order of a few months. However, adjustment timescales have been found to be largely model dependent, ranging from a month to a decade (Marshall and Johnson, 2013). These differences are often explained by numerical effects owing to resolution and grid type, but Marshall and Johnson (2013) suggest that it is instead because the Kelvin waves only are important for high frequency variation. On timescales longer than a few months, it is instead short Rossby waves that dominate the signal propagation along the western boundary. Marshall and Johnson (2013) find that the boundary Rossby wave signal is highly dependent on model parameters and ability to resolve boundary layers as the propagation speed is inversely proportional to boundary layer width, which would explain the large variation in AMOC adjustment timescales across models.

The model dependent signal propagation speed in GCMs also raises questions about the relative importance of boundary waves compared to advection in terms of propagating the buoyancy anomalies southwards. GCM studies by Buckley *et al.* (2012), Marotzke and Klinger (2000), and Zhang (2010) find advection to be the dominant process in setting the southward propagation time, with timescales on the order of several years to decades. In the latter study, which studies the AMOC in density space, it is found that the relative importance of advection and boundary waves is latitude dependent, with advection dominating in the subpolar region and boundary waves in the subtropical region (Buckley and Marshall, 2016; Zhang, 2010).

If the buoyancy anomaly does not originate in proximity to the western boundary, there is also a question of how the signal reaches the boundary in the first place. Buckley *et al.* (2012) and Marshall and Johnson (2013) suggest that the signal is communicated by Rossby waves that propagate westwards through the interior, while according to (Johnson *et al.*, 2019) they are transported from the region of deep convection by lateral eddy fluxes.

2.6 Western boundary current upwelling

Although this thesis predominantly focuses on the NADW formation and subsequent southward signal propagation at depth, I will also briefly consider

the upwelling branch of the circulation necessary for closing the loop. In the real ocean, there are two physical mechanisms thought to drive the upwelling, and thus the AMOC as a whole: vertical mixing processes in the interior, and wind-induced Ekman upwelling in the Southern Ocean (Kuhlbrodt *et al.*, 2007). This thesis considers a situation with no surface wind stress, and so the former mechanism is the focus here. The classical picture of this process is that of the Stommel-Arons model, where water downwells in localized regions at subpolar latitudes, but upwells in a nearly uniform manner over broad lateral scales (Pedlosky, 1996; Vallis, 2017). The transport of tracer C is then governed by a vertical advection-diffusion balance

$$w\frac{\partial C}{\partial z} = \frac{\partial}{\partial z}\left(\kappa\frac{\partial C}{\partial z}\right), \tag{2.38}$$

where w is the vertical velocity, and κ is the vertical turbulent diffusion coefficient (Kuhlbrodt *et al.*, 2007).

In a model of near uniform upwelling of the interior, κ is set to a constant value. However, observations indicate that κ is highly variable in space (Kuhlbrodt *et al.*, 2007). Stöber *et al.* (2008) find that the turbulent diffusivity is elevated in the WBC. However, in coarse-resolution models, excessive upwelling in the WBC is pointed towards as a cause of too weak poleward heat transport in the North Atlantic, as it acts as a short-cut for the MOC (Huck *et al.*, 1999). Huck *et al.* (1999) suggest that the upwelling in the WBC is governed by lateral boundary layer dynamics in the coarse models. This indicates that he parameterization of boundary layers plays and important role in properly representing the upwelling and thus the AMOC as a whole.

Methods

3

3.1 Model domain and setup

The processes of deep convection and subsequent adjustment of the MOC will be studied using Veros, a purely Python-based primitive equation finite-difference ocean model defined on a staggered Arakawa C-grid, as described in Häfner *et al.* (2018). Veros is based on the pyOM2-model, described in Eden (2014). Hydrostatic approximation is applied, and static instabilities are removed by automatic convective adjustment, using a TKE parameterization as described in Gaspar *et al.* (1990).

Mesoscale eddies play an important role in the spreading of convected water masses, as described in section 2.2.5. Veros implements a closure for mesoscale eddies that follows Gent *et al.* (1995), which will be applied for all experiments. Here, tracers are mixed laterally along neutral surfaces as well as advected by an effective transport velocity. The effective transport velocity is the sum of the large-scale velocity and the parameterized eddy-induced transport velocity. The isoneutral mixing is implemented following Griffies (1998), either with a constant isoneutral diffusivity K_{iso} or with diffusivities given by the prognostic EKE eddy mixing closure as described in Eden and Greatbatch (2008). The eddy-induced transport velocity is calculated in terms of a skew-diffusive flux, also following Griffies (1998), either with constant skew diffusivity K_{gm} or with skew diffusivities given by the prognostic EKE closure.

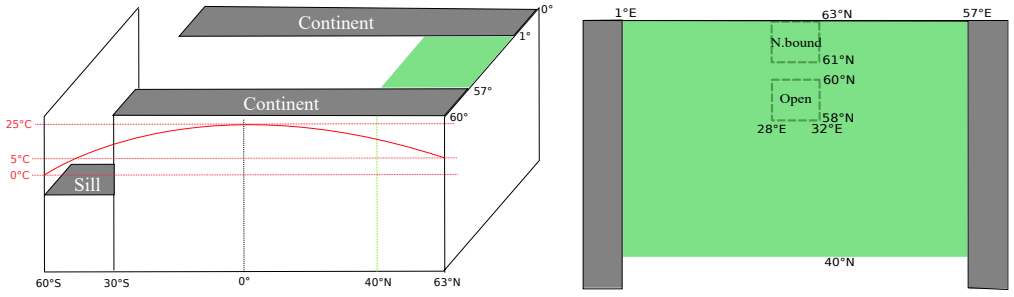

Figure 3.1.: (Left) Schematic of model basin. Red lines illustrate distribution of surface heat forcing, while the green rectangle shows the region of uniform surface salinity forcing. (Based on Figure 5 in Hansen (2023).) (Right) Regions of additional forcing used in experiments indicated by dashed squares (not to scale).

The model domain is an idealized version of the Atlantic ocean based on the model described in Andreasen (2019), made up of a box-shaped basin with a channel in the south, as shown in Figure 3.1. The domain spans from $60°$S to $63°$N in the meridional direction. The width is 60 degrees in the zonal direction and the depth is 4000 m. A sill of depth 2000 m is located between $60°$S and $30°$S. The system has periodic boundary conditions above the sill in the southern ocean, forming a channel analogous to the Drake passage. The model will be run with both a $1°$ low horizontal resolution configuration and a $\frac{1}{6}°$ high horizontal resolution configuration. The vertical resolution is the same in all experiments, defined using one-sided Vinokur-stretching with 40 levels and a minimum step size of 10 m towards the surface, with vertical resolution decreasing downwards.

Since the aim of this thesis is to investigate the effects of localized buoyancy forcings at high latitudes, the model will be purely buoyancy-forced with no surface wind stress. A combination of surface heat forcing and surface salinity forcing contribute to the total buoyancy forcing. As in the model of Andreasen (2019), the surface heat forcing is described by the temperature profile

$$T(\theta) = \begin{cases} T_s + \Delta T \sin\left(\pi \frac{\theta + 60°}{120°}\right), & \text{if } \theta < 0° \\ T_n + (\Delta T + T_s - T_n) \sin\left(\pi \frac{\theta + 60°}{120°}\right), & \text{if } \theta > 0°, \end{cases} \tag{3.1}$$

where θ is the latitude, $T_s = 0°$C is the temperature at the southern boundary, $T_n = 5°$C is the temperature at the northern boundary, and $\Delta T = 25°$C is the temperature at the equator. The resulting sinusoidal shape of the temperature profile is illustrated by the solid red line in Figure 3.1, and the restoring timescale of the temperature is set to $\tau_T = 10$ days. The entire ocean is initialized with a uniform salinity of $S_0 = 35$ g/kg, and is then forced with a uniform surface salinity-profile set to $S_n = 36$ g/kg in the region north of $40°$N, as shown in Figure 3.1. The restoring timescale of the salinity is set to $\tau_S = 30$ days. While a northern region of increased surface salinity is the opposite of what is observed in the real Atlantic Ocean (Reverdin *et al.*, 2007), it is an effective way of ensuring a northern sinking region and a sufficiently strong northern overturning cell. Therefore, I have deemed it an appropriate choice for my experiments. The uniform surface salinity forcing also ensures a weakening of the upper layer stratification at high latitudes, mimicking real ocean preconditioning in regions of open-ocean convection.

3.2 Experiments

The aim of this thesis is to explore the short-term and long-term consequences of imposing a strong spatially localized buoyancy forcing at high latitudes. The long-term consequences (scales of decades to centuries) are tested in four main experiments, characterized by variation in lateral viscosity, adjacency to vertical boundaries and representation of mesoscale eddies. Details of each long-term experiment are given below and are summarized in Table 3.2. In addition to the four main experiments, three sets of short-term experiments (scales of days to one year) are conducted in order to test the theory for mixed patch dynamics described in 2.2.5. The sets of short-term experiments are described in 3.2.3 and summarized in Table 3.3.

3.2.1 Spin-up configurations

The model is spun up with four different configurations, summarized in Table 3.1. The first configuration, hereafter referred to as standard (*std.*), has 1° horizontal resolution, constant isoneutral-diffusivity $K_{iso} = 1000$ m^2/s and skew-diffusivity $K_{gm} = 1300$ m^2/s, and lateral viscosity $A_h = 5 \times 10^4$ m^2/s. In the second configuration, hereafter *EKE*, K_{iso} and K_{gm} are determined according to the prognostic EKE eddy-closure by Eden and Greatbatch (2008). Otherwise, everything is kept the same as in *std.* The third configuration, hereafter *Low A_h*, lowers the lateral viscosity to $A_h = 5 \times 10^2$ m^2/s. Everything else is kept identical to *std.* In the fourth , hereafter high-resolution (*HR*), the horizontal resolution is increased to $1/6^\circ$. To account for the increased resolution, K_{iso} and K_{gm} are both decreased, while a biharmonic viscosity A_{hbi} is introduced to reduce grid-scale noise and spurious upwelling near vertical boundaries (see Appendix A). Otherwise, all other parameters are kept the same as in the standard configuration.

The three low-resolution configurations (*std., EKE, low A_h*) are each spun up for 100 years. *HR* is only spun up for 15 years due to resource constraints as well as numerical issues that cause unrealistically strong overturning near the equator that begins dominating the circulation after approximately 20 years (see Appendix A). For this reason, *HR* will only be used to analyse local properties of the mixed patch in the short-term experiments, as well as upwelling in the western boundary current, both for which the conditions after 15 years should be sufficiently stable.

Configuration	std.	EKE	Low A_h	HR
Horizontal resolution	1°	1°	1°	$1/6^\circ$
A_h [m^2/s]	5×10^4	5×10^4	5×10^2	5×10^4
K_{iso} [m^2/s]	1000	EKE	1000	160
K_{gm} [m^2/s]	1300	EKE	1300	160
A_{hbi} [m^4/s]	–	–	–	10^{10}
Spin-up time [years]	100	100	100	15

Table 3.1.: Spin-up configurations. Variables are explained in 3.2.1

Experiment	Open [std.]	N.bound [std.]	Open [EKE]	Open [low A_h]
Lat. [°N]	$[58, 60]$	$[61, 63]$	$[58, 60]$	$[58, 60]$
Long. [°E]	$[28, 32]$	$[28, 32]$	$[28, 32]$	$[28, 32]$
S_f [g/kg]	44.5	44.5	44.5	44.5
$S_{surf,init}$ [g/kg]	35.60	35.64	35.61	35.67
$\mathscr{B}_0$ [10^{-7} m^2/s^3]	3.07	3.25	3.02	3.07
MLD_0 [m]	1389	3885	1690	2575
Ro^*	0.29	0.10	0.23	0.15
N [10^{-4} s^{-1}]	2.67	–	1.65	2.47

Table 3.2.: Long-term experiments, forcing region and initial parameters. Variables are explained in 3.2.2.

3.2.2 Long-term experiments

Four different long-term experiments are conducted, all using 1° horizontal resolution: (1) *Open [std.]*, (2) *N.bound [std.]*, (3) *Open [EKE]* and (4) *Open [low A_h]*. Names in square brackets refer to their respective spin-up configurations. *Open* and *N.bound* refers to the location of additional salinity forcing, where *Open* is separated from any vertical boundaries while *N.bound* is in contact with the northern boundary. Exact locations are given in Figure 3.1 and Table 3.2. The unperturbed configurations are kept running throughout the runtime of the experiments, and will be referred to as *Ctrl [std.], Ctrl [EKE]* and *Ctrl [low A_h]*.

In each experiment, buoyancy forcing is imposed in the form of a strong surface reference salinity S_f over a $2^\circ \times 4^\circ$ region, or roughly 222 km×222 km. This induces a strong surface salinity flux into the ocean, and thus a negative buoyancy flux. This is analogous to the strong surface cooling that is usually the source of buoyancy flux in real open-ocean convection. It should be noted that treating buoyancy forcing by heat and salinity fluxes as equivalent is not entirely accurate, as temperature and salinity have different model boundary conditions (restoration timescales are 10 and 30 days respectively),

and contribute differently to the equation of state, as discussed in 2.3. For the analysis at hand, however, the convenience of adding easily traceable salt outweighs the disadvantage of reduced applicability to realistic open-ocean convection.

The magnitude of S_f over the mixed patch is chosen relative to the initial surface salinity $S_{surf,init}$ so that the initial buoyancy flux is comparable to observed magnitudes during open-ocean convection, which can be larger than $\mathscr{B}_0 \sim 10^{-7}$ m^2/s^3 (Marshall and Schott, 1999). The Rossby number Ro^* is also taken into account when deciding S_f. The purpose of this it to obtain realistic values for oceanic deep convection, considering the importance of rotational effects. For convenience, all 1° are given the same S_f, meaning $\mathscr{B}_0$ and Ro^* will differ slightly due to differences in surface salinity and mixed layer depth at the initial time of the forcing. Given S_f and calculated values for $\mathscr{B}_0$ and Ro^* are given in Table 3.2, where $\mathscr{B}_0$ is found using (2.16) with model output for surface salinity and temperature forcing. Ro^* is found using initial mixed layer depth MLD_0, which is chosen to be the uppermost depth where the potential density deviates from the surface density by 0.01 kg/m^3 or more. Note that measuring the MLD using only difference in potential density has its flaws, and may over-estimate the depth of the mixed layer in deep convective regions (Courtois *et al.*, 2017). Applying more sophisticated methods of MLD measurement is outside the scope of this thesis, but it is still something to keep in mind.

Comparison of *Open [std.]* and *N.bound [std.]* is motivated by the expectation that convection next to a vertical boundary will break the geostrophic constraints on vertical velocities and Eulerian downwelling in the mixed patch, as discussed in sections 2.2.3 and 2.2.4. As discussed in section 2.2.6, representing the three-dimensional spatial variation of the *lateral exchange and spreading*-phase may prove a determining factor in representation of open-ocean convection in large-scale models. This hypothesis is the basis for comparison of constant K_{iso} and K_{gm} in *Open [std.]* to the varying diffusivities in *Open [EKE]*. Finally, the cases of high and low lateral viscosities are compared in order to investigate whether the difference will impact signal propagation, as higher lateral viscosities are expected to more strongly dampen wave propagation.

3.2.3 Short-term experiments

Three sets of short-term experiments are conducted, using the *std.*, *EKE* and *HR* configurations respectively. The experiments are started after the initial

	$\mathscr{B}_{0,std.}$	$\mathscr{B}_{0,EKE}$	$\mathscr{B}_{0,HR}$	$[10^{-7}\ \mathrm{m^2/s^3}]$
S38.5r$_0$	1.16	1.10	1.28	
S40r$_0$	1.63	1.58	1.68	
S40r$_1$	1.61	1.56	1.62	
S44.5r$_0$	3.07	3.02	2.89	
S44.5r$_1$	3.05	3.00	2.82	
S44.5r$_2$	–	–	2.85	
S50r$_0$	4.83	4.78	4.37	
S50r$_1$	4.81	4.75	–	
S55.5r$_0$	6.59	6.53	5.84	

Table 3.3.: Short-term experiments, initial buoyancy flux.

	r_0	r_1	r_2
Lat. [°N]	$[58, 60]$	$[58, 60]$	$[58, 59]$
Long. [°E]	$[28, 32]$	$[29, 31]$	$[29.5, 30.5]$
r [km]	136.2	68.6	34.2

Table 3.4.: Forcing regions of short-term experiments.

spin-up time of the given configuration as given in Table 3.1, and run for one year with daily averages as output. In the experiments, S_f and the area of the forcing region is varied. This is with the purpose of testing the predicted scaling relations for quasi-equilibrium depth and timescale of the mixed patch, as given by (2.29) and (2.32). The experiments are summarized in Table 3.3. The experiments are named on the format SXr$_n$, where X indicates the magnitude of the surface reference salinity S_f, while $n = \{0, 1, 2\}$ indicates forcing area, given in Table 3.4. The theory in 2.2.5 is developed in terms of a circular forcing area, while in the experiments the area is rectangular. The radii r of the three forcing regions that will be applied in (2.29) and (2.32) is therefore taken to be the average of the radii of the inscribed and circumscribed circles of the forcing area, and are given in Table 3.4. The same theory is also developed with the assumption that the buoyancy frequency N is constant, which is not the case here. Instead, N is taken to be the initial mean buoayncy frequency over the entire column depth and area of the mixed patch. This gives $N_{std.} = 2.67 \times 10^{-4}\mathrm{s}^{-1}$, $N_{EKE} = 1.65 \times 10^{-4}\mathrm{s}^{-1}$, and $N_{HR} = 5.4 \times 10^{-4}\mathrm{s}^{-1}$.

Results & analysis

4

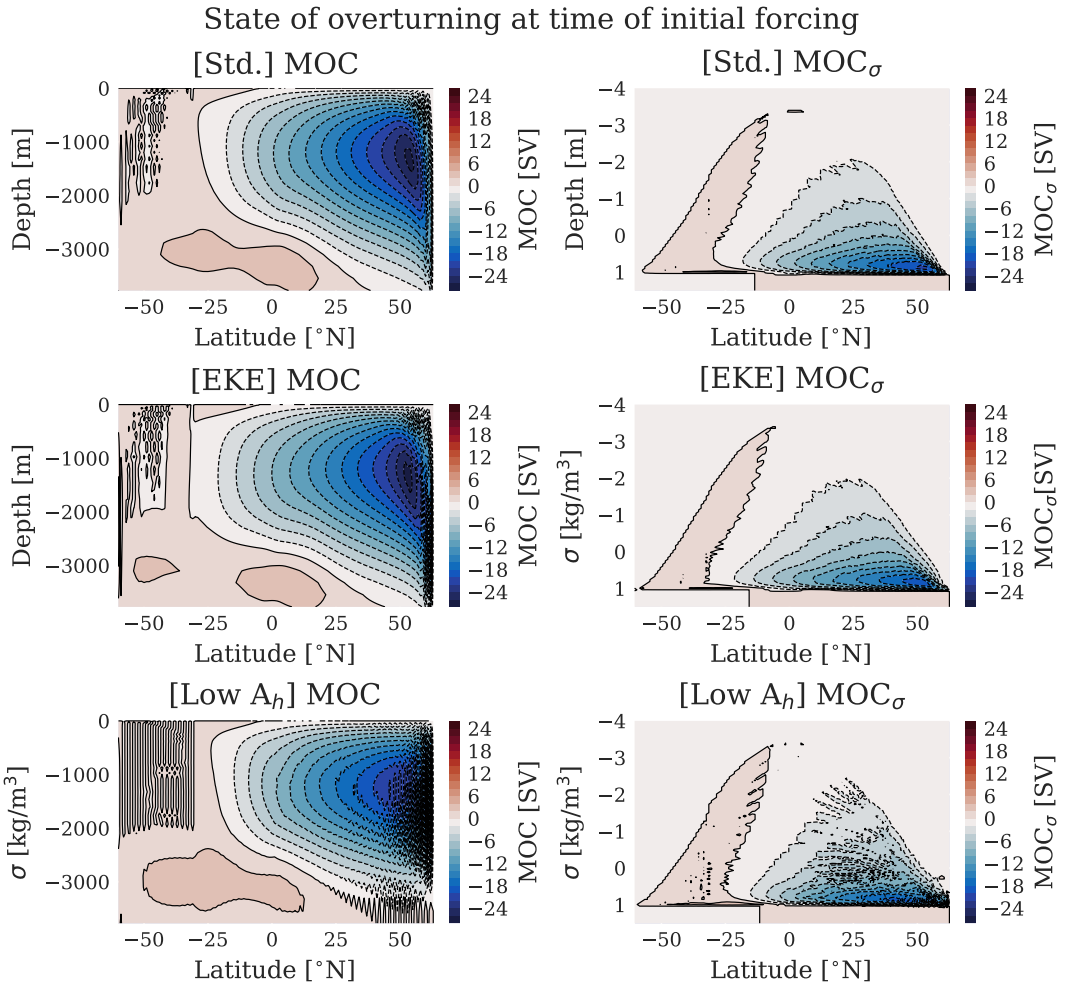

Figure 4.1.: State of overturning after 100 years spin-up in depth space (left) and density space (right) for each of the three 1° spin-up configurations.

4.1 Spin-up and unperturbed state of the AMOC

Figure 4.1 shows the unperturbed state of the overturning circulation in depth space and density space for each of the three low resolution configurations, following 100 years of spin-up. All configurations exhibit similar large-scale structure and strength, with a strong overturning cell concentrated in the northern hemisphere, stretching just across the equator and with its peak strength between 1000 and 2000 meters depth. Negative values indicate that the circulation is clockwise. All three configurations also show signs of a

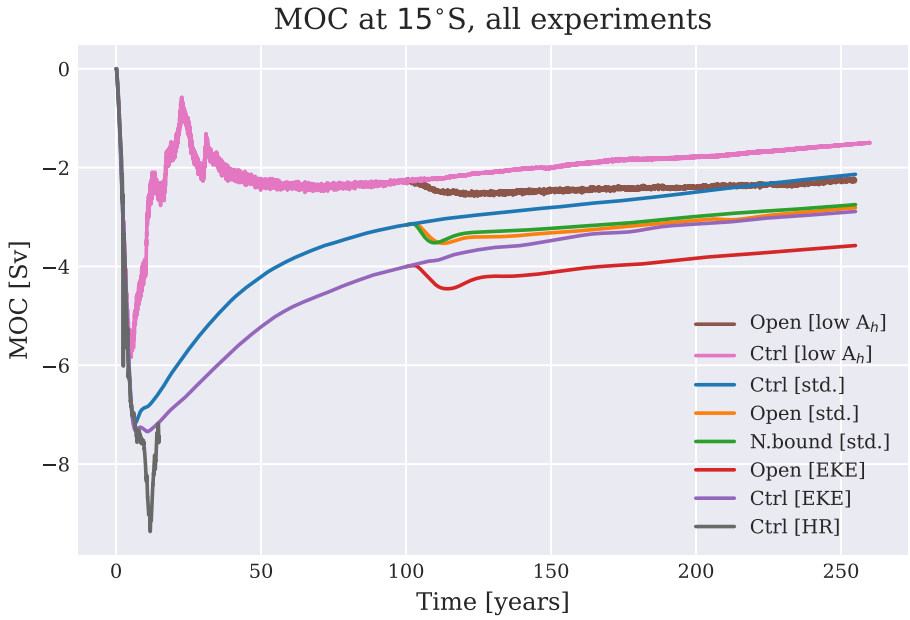

Figure 4.2.: Strength of MOC ($\Psi_{max}(\phi, t)$) at 15°S for all low resolution runs, including spin-up. Localized forcing is initiated after 100 years. More negative values indicate stronger overturning.

much weaker southern cell of opposite overturning, located in the deep abyss. In density space, it is clear that the strongest circulation is located between $\sigma = 0$ kg/m^3 and $\sigma = 1$ kg/m^3 (where σ is the anomaly from the surface reference density of 1024 kg/m^3). As expected, *low* A_h is showing more noise than the two other configurations. Another thing to notice is that the northern overturning cell in *EKE* seems to maintain its strength slightly further south across the equator than the other two configurations. The overturning stream function in depth space is given by Veros diagnostics, while the overturning stream function in density space is found according to (2.34).

The strength of the MOC at a given latitude is taken to be the largest absolute value of the overturning stream function at that latitude. This means that, for the northern overturning cell, this would be the most negative value. To evaluate the large-scale consequences of a localized forcing at high latitudes, the strength of the MOC should be measured sufficiently far away from the forcing region, so that local processes have as little impact as possible. I chose the latitude band at 15°S because this is as far south as possible while still being well within the range of the northern overturning cell, as shown in Figure 4.1. Figure 4.2 shows the strength of the MOC at 15°S for the spin-up of each configurations, as well as for the forced- and unperturbed control runs

following the onset of the localized forcing at 100 years. It appears that all three low-resolution configurations sufficiently reach steady state within the first 100 years. In steady state, the strength of the three configurations differ at scales of around a Sverdrup. The high-resolution configuration does not show the same convergence towards steady-state, as is discussed in Appendix A.

One issue to note is that the different configurations may treat equatorial processes differently, so that differences between the experiments at 15°S may be caused by differences in how signals cross the equator, rather than by differences in how the open-ocean convection is represented. Details of the equatorial crossing is outside of the scope of this thesis, but this issue is nevertheless a relevant point to take note of.

4.2 Mixed patch development

4.2.1 Low resolution

The focus is now turned to the mixed patch scale, and the short-term response to the localized forcing. For each of the main four low-resolution experiments, Figure 4.3 shows potential density of the localized forcing region and its surroundings averaged over the meridional coordinates of the region, at select timestamps following the onset of the experiment. Figure 4.4 shows the same, but in terms of salinity anomaly compared to the corresponding control run, while Figure 4.5 shows salinity anomaly in zonal direction, averaged over the zonal coordinates of the localized forcing region. The figures illustrate how the fluid transformed at the surface spreads vertically and laterally. The factor that most notably changes the spreading pattern is whether or not the forcing happens near a vertical boundary, as *N.bound [std.]* clearly differs strongly from the three other experiments. Here, mixing throughout the entire water column can be seen within the first 45 days, while spreading in lateral direction seems to mainly occur along the ocean bottom. In contrast, all three experiments in open ocean show a larger degree of lateral spreading, and do not mix downwards as rapidly or to as large a degree as *N.bound [std.]*. Note however that the conditions before the forcing is initiated are already very different near the northern boundary compared to the open ocean, with negligible vertical stratification.

Figure 4.6 shows a comparison of vertical velocities averaged horizontally over the forcing regions of *Open [std.]* and *N.bound [std.]*, showing that

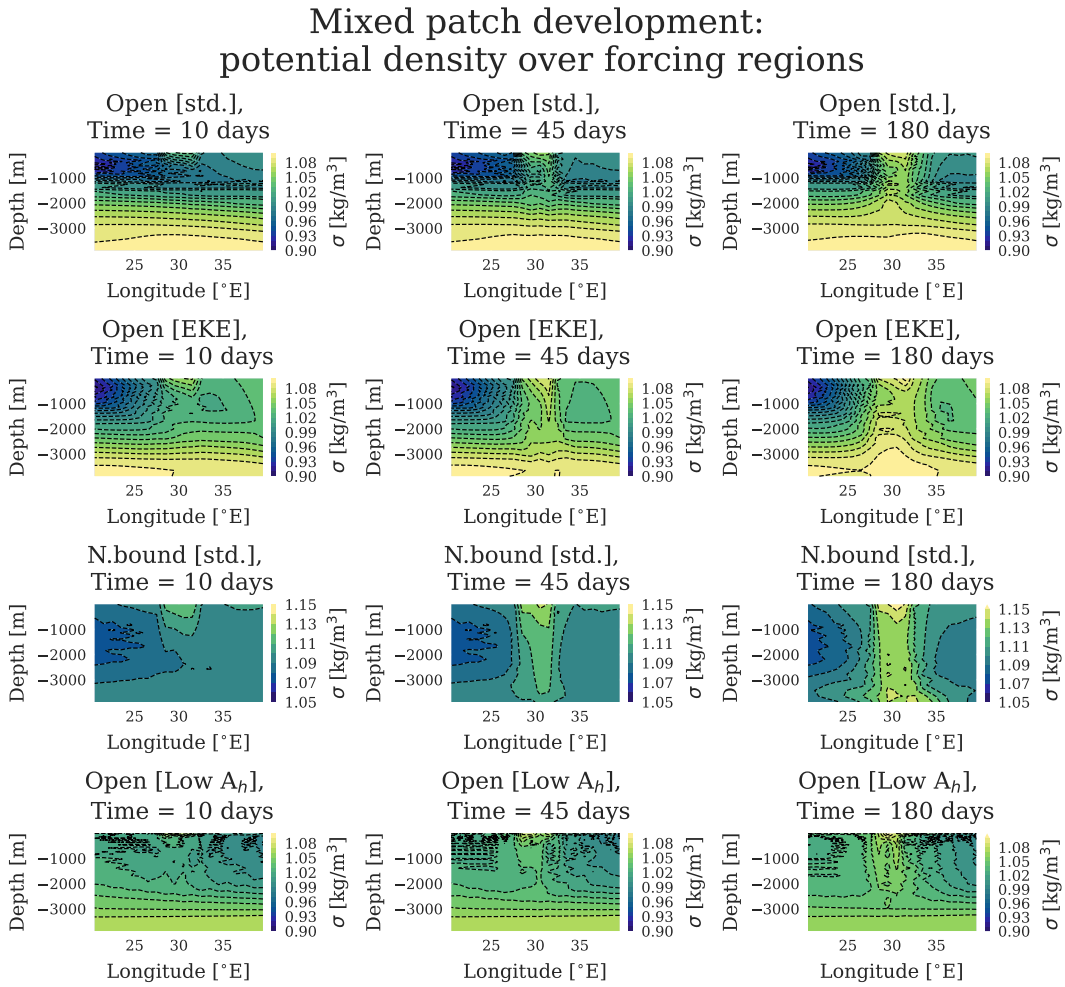

Figure 4.3.: Potential density of mixed patch and surroundings, averaged over the meridional coordinates of the mixed patch as given in Table 3.2. Time is in days after localized forcing is initiated. Contour line spacing is 0.01 kg/m^3.

peak vertical velocities are roughly three times larger when the forcing is next to the northern boundary. The larger vertical velocities and more rapid vertical mixing with less lateral spreading seem to support the suggestion that a vertical boundary can break constraints set by the potential vorticity balance, as discussed in 2.2.4. However, vertical velocities in both cases are very small.

Open [EKE] mixes deeper than *Open [std.]*, and shows weaker salinity anomalies near the surface of the mixed patch, indicating that the added salinity is to a larger degree distributed away from the near surface. Note however that the initial mixed layer is deeper and the initial stratification is weaker, as given in Table 3.2.

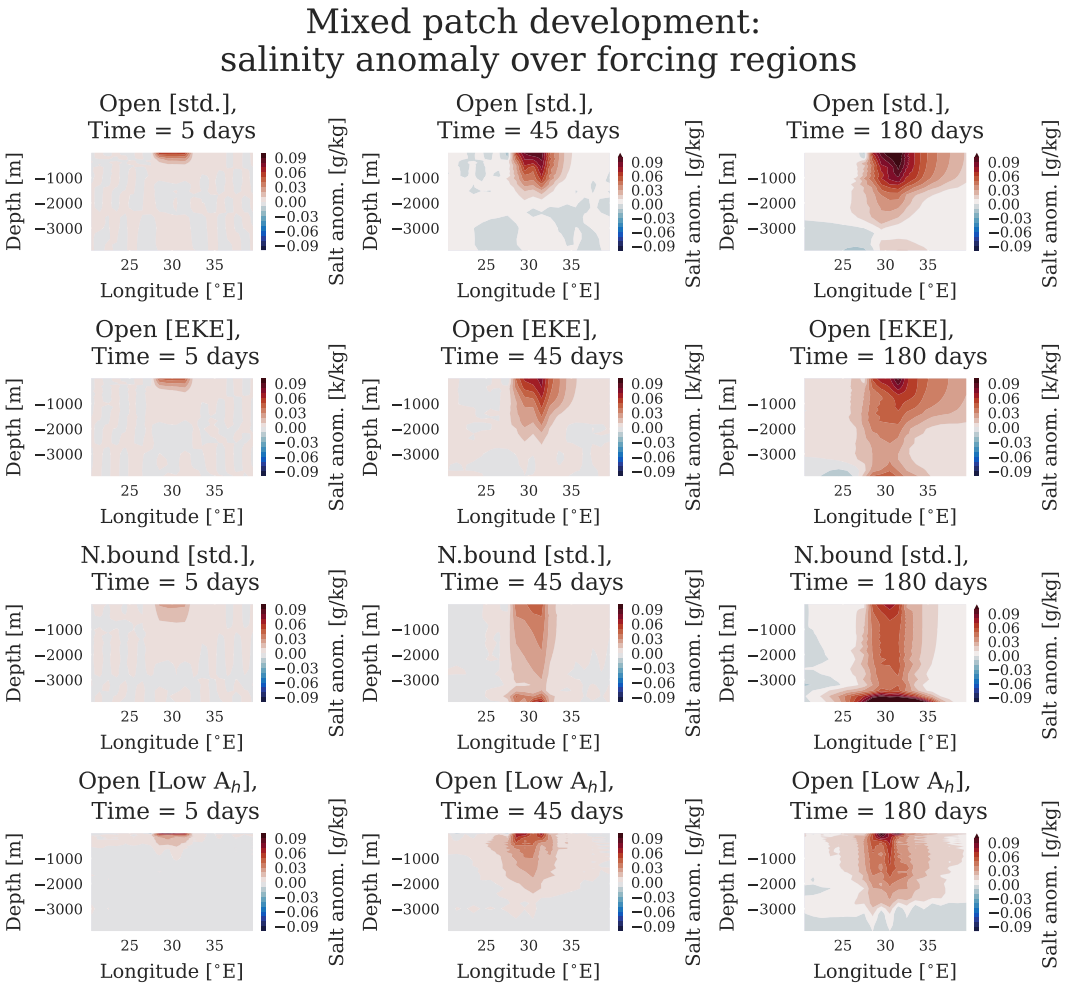

Figure 4.4.: Salinity anomaly (deviance from control run) of mixed patch and surroundings, averaged over the meridional coordinates of the mixed patch as given in Table 3.2. Time is in days after localized forcing is initiated. Contour line spacing is 0.01 g/kg.

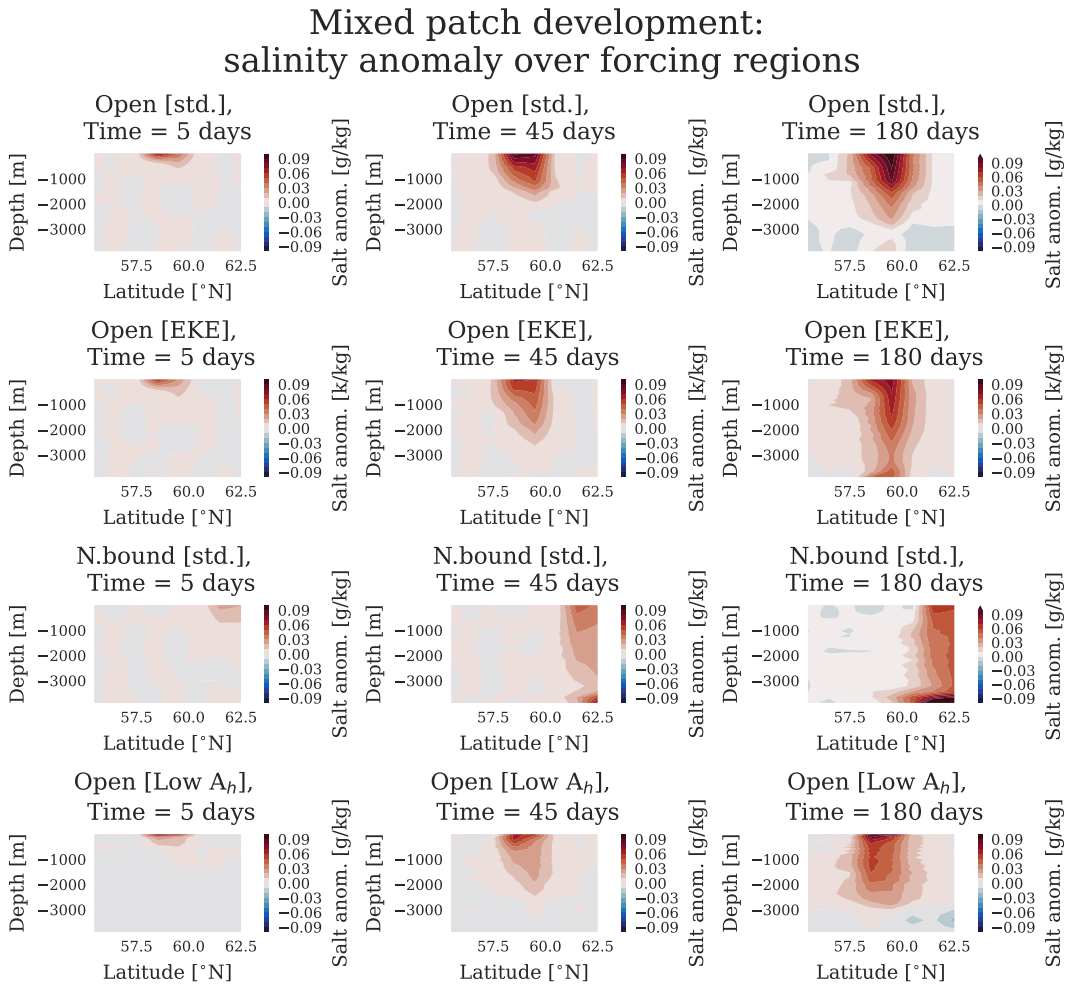

Figure 4.5.: Salinity anomaly (deviance from control run) of mixed patch and surroundings, averaged over the zonal coordinates of the mixed patch as given in Table 3.2. Time is in days after localized forcing is initiated. Contour line spacing is 0.01 g/kg.

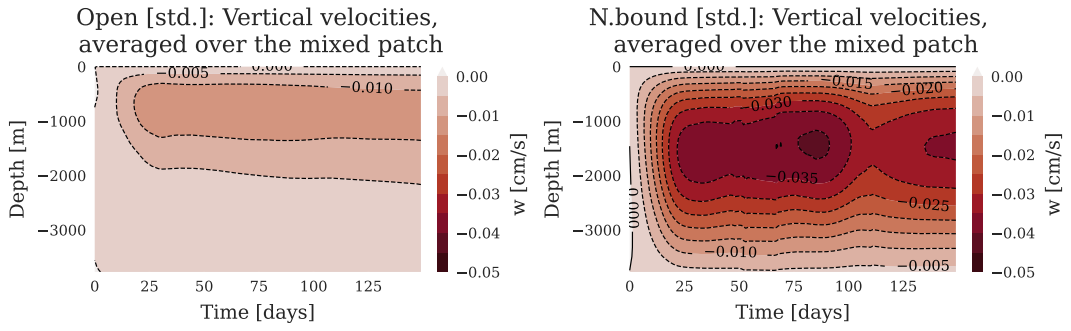

Figure 4.6.: Comparison of vertical velocities in open-ocean convection compared to convection adjacent to boundary. Vertical velocitites are averaged over the area of the respective mixed patches. Time is in days after onset of localized forcing.

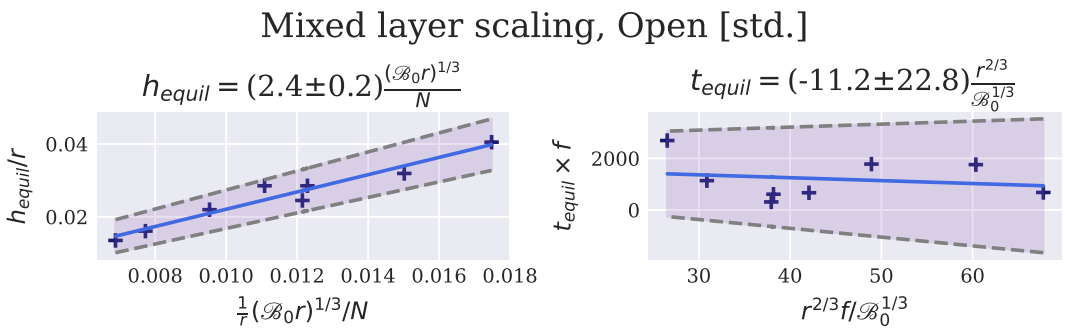

Figure 4.7.: *Open [std.]:* (Left) Linear regression of mixed patch depth at quasi-equilibrium versus predicted depth h_{final} according to (2.29), both normalized by mixed patch radius. (Right) Linear regression of time taken for mixed patch to reach quasi-equilibrium depth, versus predicted time t_{final} according to (2.32), both normalized by f. Data points from experiments described in Table 3.3. Dashed lines show standard error range.

Using the sets of short-term experiments with the *std.* and *EKE* configuration described in 3.2.3, Figures 4.7 and 4.8 test the theoretical scaling relation given in 2.2.5. As before, the MLD is defined to be where the uppermost depth where the potential density σ deviates from the surface potential density by more than 0.01 kg/m^3. If the MLD remains stable for at least $t_{req} = 100$ days, the mixed patch is defined to be in quasi-equilibrium, with h_{equil} equal to the stable MLD, and t_{equil} set to the time the system first reaches the stable MLD. Following Visbeck *et al.* (1996), the observed and predicted equilibrium depths are normalized by the radius of the forcing region r, while the observed and predicted equilibrium times are normalized by the rate of rotation f.

For h_{equil}, (2.29) seems to hold well, with clear correlation between predicted and observed equilibrium depths. I find remarkable agreement for the proportionality constant γ between *Open [std.]* and *Open [EKE]*, with $\gamma_{std} = 2.4 \pm 0.2$ and $\gamma_{EKE} = 2.3 \pm 0.2$. This indicates similar efficiency of baroclinic eddy transfer between the mixed patch and its surroundings for *std.* and *EKE*.

On the other hand, for *Open [std.]*, the observed equilibrium timescales show negative correlation with the predictions from (2.32), and with large standard errors, $\beta_{std.} = -11 \pm 23$. *Open [EKE]* shows positive correlation, but with similarly large error ranges, with $\beta = 14 \pm 22$. The large differences could be linked to the somewhat arbitrarily set t_{req} used to determine when the system mixed patch has reached quasi-equilibrium. Furthermore, in deriving (2.32), several assumptions are made that do not hold in the experiments at hand. Most notably the assumption of constant stratification N in the derivation

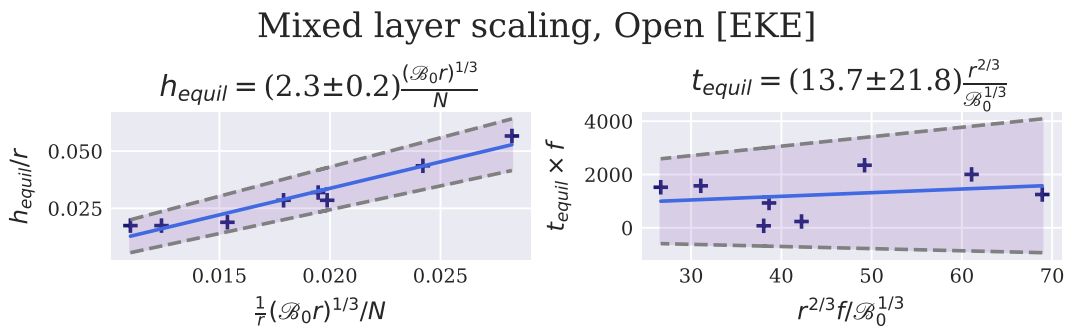

Figure 4.8.: *Open [EKE]:* (Left) Linear regression of mixed patch depth at quasi-equilibrium versus predicted depth h_{final} according to (2.29), both normalized by mixed patch radius. (Right) Linear regression of time taken for mixed patch to reach quasi-equilibrium depth, versus predicted time t_{final} according to (2.32), both normalized by f. Data points from experiments described in Table 3.3. Dashed lines show standard error range.

of the mixed layer deepening, (2.31). This is certainly not the case in the experiments, as can be seen in Figure 4.3. Another issue is that the buoyancy loss $\mathscr{B}_0$ at the surface is not constant throughout the experiment, but changes as the surface salinity adjusts.

Figures 4.9 and 4.10 show the difference between potential density at depth and the surface potential density, averaged over the area of the forcing region, for the first year after onset of the experiment. The observed mixed layer is shown with a solid line, the predicted equilibrium depth h_{equil} using γ_{std} and γ_{EKE} is given by the dash-dotted line, along with its range. The dotted line shows the predicted mixed layer deepening $h(t)$ according to (2.31), while the dashed line $h(t)^*$ shows the same but with the proportionality constant Λ adjusted by eye to roughly fit the observed development. Due to the large error ranges for $\beta_{std.,EKE}$, the predicted t_{equil} is not shown.

In the case of *Open [std.]*, it is clear that the observed mixed layer deepening is slower than what is predicted according to (2.31). However, when adjusting the proportionality constant from the theoretically derived value $\Lambda = \sqrt{2}$ to $\Lambda = 0.5$, the shape of the adjustment largely agrees with the analytical result, until quasi-equilibrium is reached at $MLD = 2991$ m after 165 days.

For *Open [EKE]*, the adjustment of the MLD to the forcing shows different behaviour. Here, the initial adjustment is rapid, and closely follows the theoretically predicted $h(t)$ during the first days, before slowing down after roughly 25 days. Maximum depth is reached after roughly 75 days, before

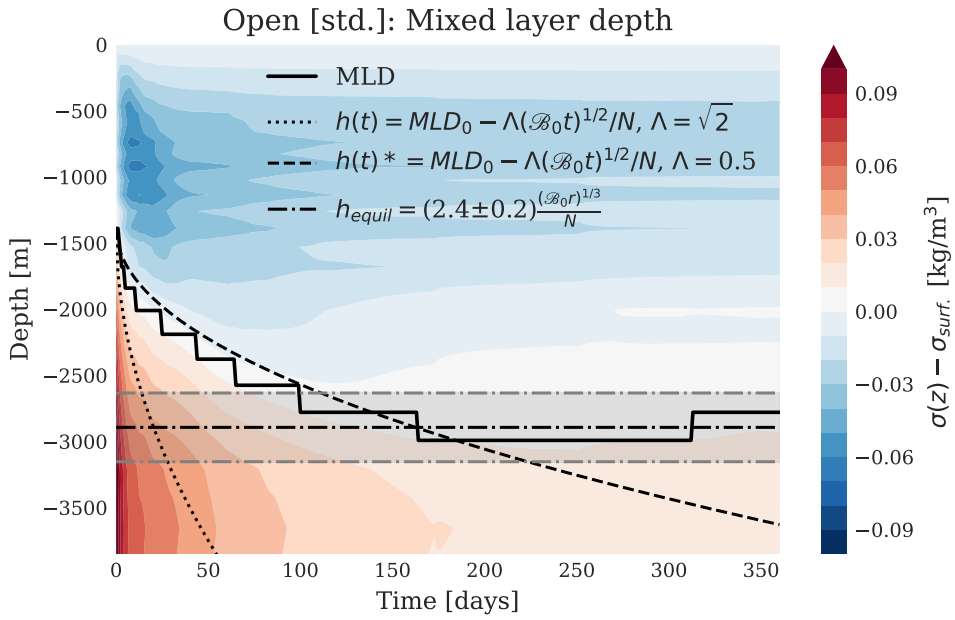

Figure 4.9.: *Open [std.], S44.5r$_0$*: Predicted and observed MLD. Contours show difference between potential density at depth and surface potential density. Solid line shows observed MLD. Dash-dotted line shows predicted h_{equil} using $\gamma_{std.}$ found in Figure 4.7, with uncertainty range. Dotted line shows predicted mixed layer deepening $h(t)$ as given by (2.31), dashed line shows adjusted mixed layer deepening $h(t)^*$ with constant of proportionality Λ adjusted by eye to fit the observed MLD.

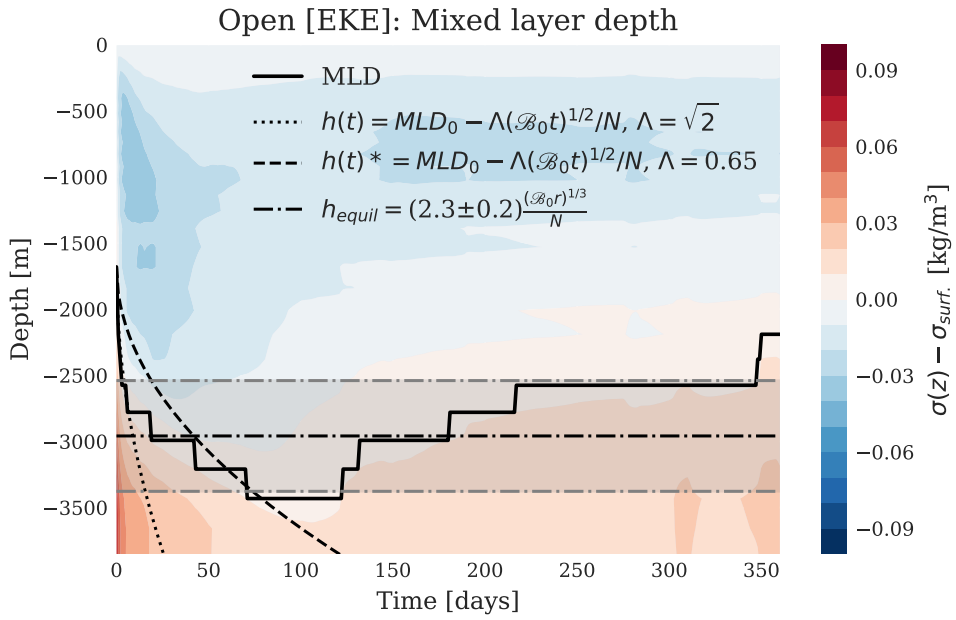

Figure 4.10.: *Open [EKE]: S44.5r_0*: Predicted and observed MLD. Contours show difference between potential density at depth and surface potential density. Solid line shows observed MLD. Dash-dotted line shows predicted h_{equil} using γ_{EKE} found in Figure 4.8, with uncertainty range. Dotted line shows predicted mixed layer deepening $h(t)$ as given by (2.31), dashed line shows adjusted mixed layer deepening $h(t)^*$ with constant of proportionality Λ adjusted by eye to fit the observed MLD.

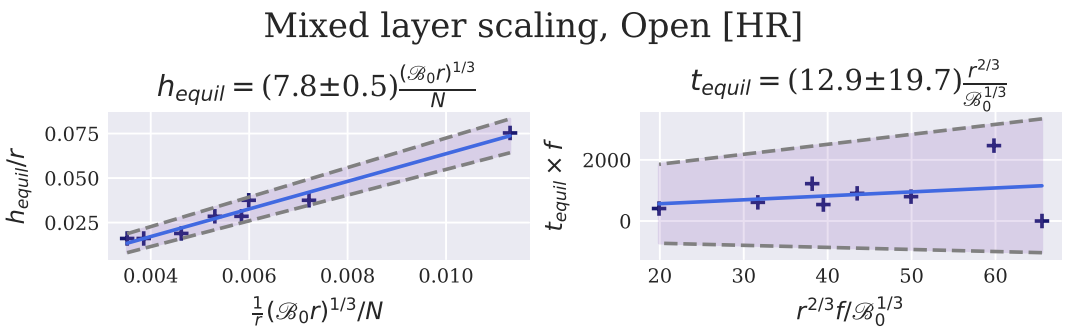

Figure 4.11.: *Open [HR]:* (Left) Linear regression of mixed patch depth at quasi-equilibrium versus predicted depth h_{final} according to (2.29), both normalized by mixed patch radius. (Right) Linear regression of time taken for mixed patch to reach quasi-equilibrium depth, versus predicted time t_{final} according to (2.32), both normalized by f. Data points from experiments described in Table 3.3. Dashed lines show standard error range.

the mixed layer readjusts and eventually settles at $MLD = 2575$ m after 218 days.

4.2.2 High resolution

The initial conditions of the *Open [HR]* experiments differs significantly from the conditions of the 1° experiments, with a deeper initial MLD of 2190 m and stronger stratification below the mixed layer. These differences may be due the eddy-permitting set-up better resolving real physical processes, but they may also stem from the short spin-up time, or they may possibly be linked to the apparent numerical issues of the *HR* set-up, discussed in Appendix A. The uncertainty caused by these issues reduce the applicability of the data, but some limited analysis may still be conducted.

First, the method for testing (2.29) and (2.32) and estimating the respective constants of proportionality γ and β can still be applied, as this analysis already accounts for differences in initial stratification. Figure 4.11 shows that the predicted and observed h_{final} correlate. The estimated constant of proportionality is found to be $\gamma_{HR} = 7.8 \pm 0.5$, indicating that the mixed layer deepening is not as effectively arrested by baroclinic eddies as in *Open [std.]* and *Open [EKE]*. For t_{equil}, the proportionality constant β_{HR} is close in value to β_{EKE}, and shows the same large standard errors as in *Open [std.]* and *Open [EKE]*.

Next, the high resolution experiment allows for a qualitative view of the details of the mixed patch that is not possible in the low resolution models. Figure

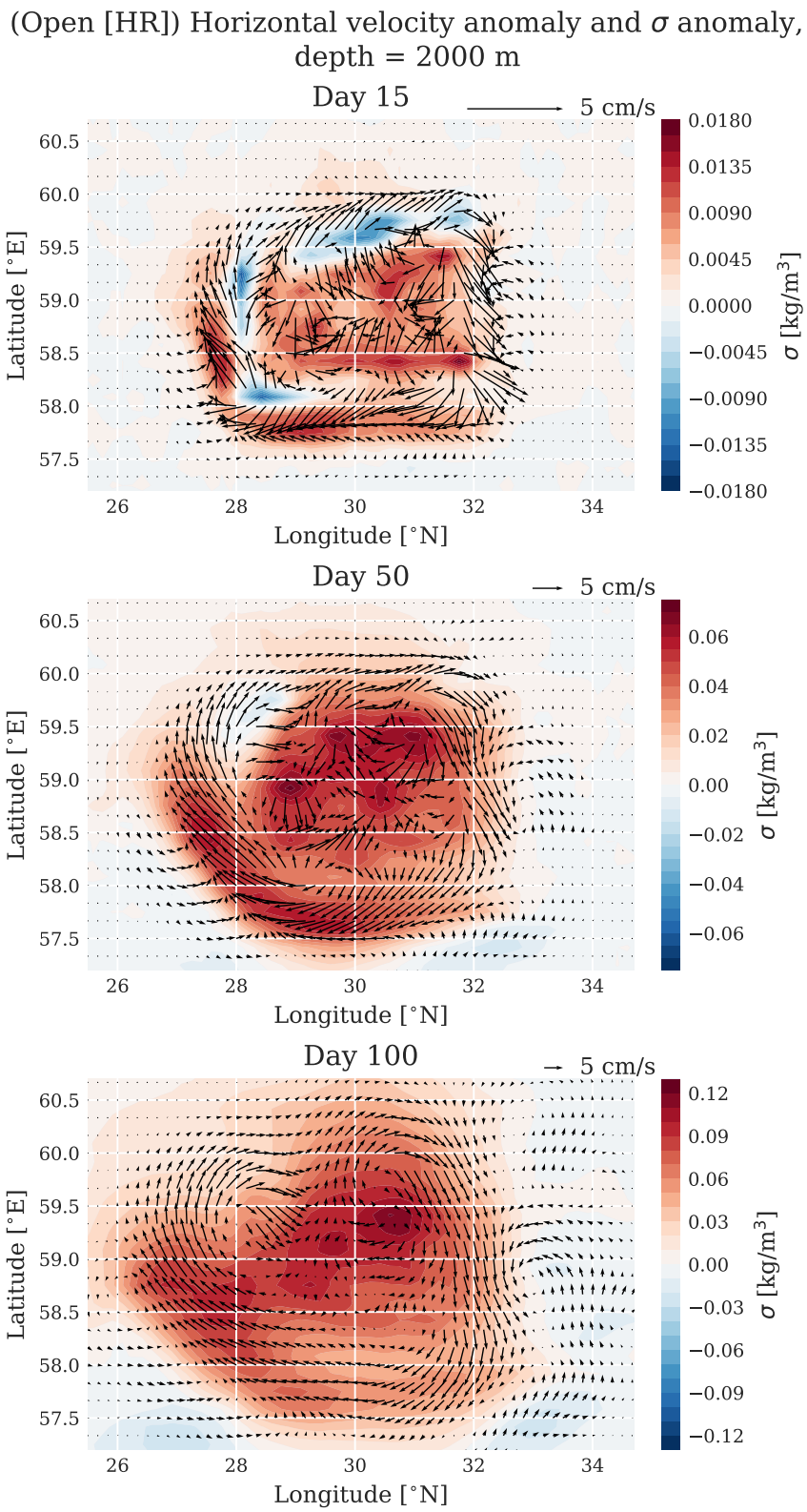

Figure 4.12.: *Open [HR]*: Top down view of the mixed patch and surrounding area near the base of the initial mixed layer, at selected times after the experiment is initiated. The vector plot shows the horizontal velocity anomalies, the contour plot shows the potential density anomalies (difference between *Open [HR]* and *Ctrl [HR]*). Note that scale reference velocity (top right corner) and scale of colorbar varies.

4.12 shows a top down view of the mixed patch in *Open [HR]* near the base of the initial mixed layer at selected times after the experiment is initiated. The vector plot shows the horizontal velocity anomalies, while the contour plot shows the potential density anomalies (difference between *Open [HR]* and *Ctrl [HR]*). Here, we can confirm that the mixed patch indeed seems to develop as expected. After 15 days, we see that mixing is occuring at the selected depth, with mostly incrase in potential density along with regions of decreased densities inbetween. After 50 days, we see that the of lower densitites have largely vanished, but the patch is still heterogeneous with some regions of higher densities. The rim-current system around the patch is developing, and appears to be meandering and shedding eddies at the edge. After 100 days, we see signs of mesoscale eddies, and we see that the dense water is clearly spreading laterally from the patch as expected.

4.3 Large-scale adjustment in density space

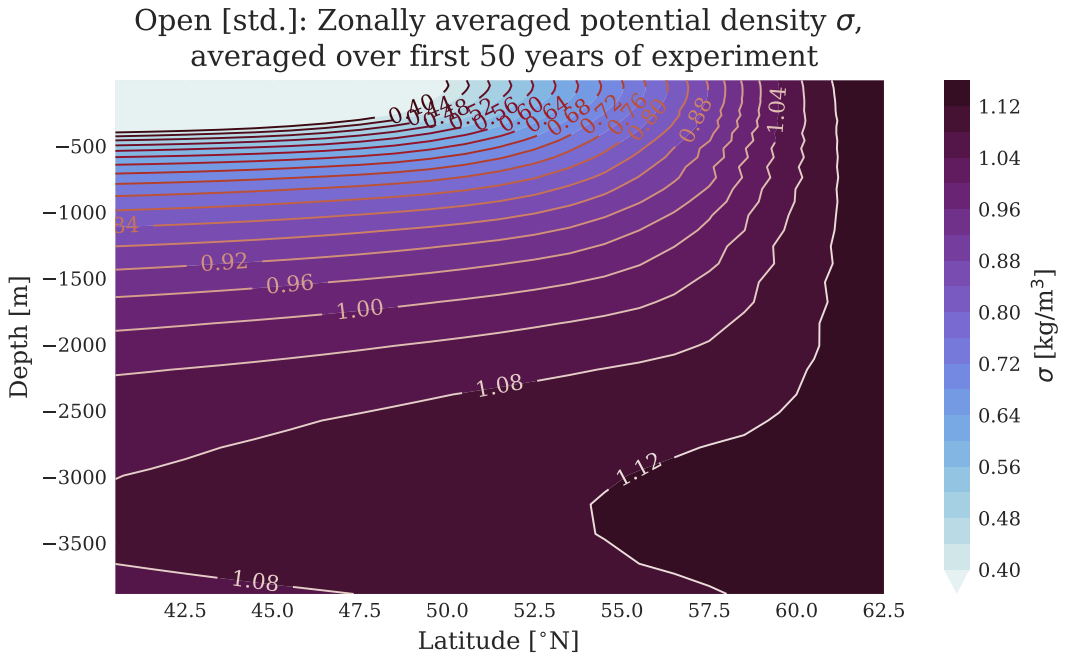

Figure 4.13.: *Open [std.]*: Zonally averaged potential densities north of 40°N, averaged over the first 50 years of the experiment.

Zooming back out to the large-scale adjustment of the overturning circulation, the focus is now turned to analysis in density space. First, to get a feeling of the relation between depth and density layers, Figure 4.13 shows zonally averaged isopycnals for *Open [std.]* in the northern region, averaged over the first 50 years of the experiment. Figures 4.14 and 4.15 show the mean

annual contributions of each term in the volume and buoyancy budget of the northern region of the domain ($\sigma > 40.5°$N), for *Open [std.]* and *Open [EKE]* respectively. The terms, as defined in (2.35) are the surface water mass transformation F, the mixing transformation G_D, the volume change $\partial V/\partial t$, and the net overturning into the region Ψ_σ, for a given potential density surface σ. The actual values for the experiments are presented, as well as the difference between the experiments and the corresponding control runs.

Focusing on F_{anom} and $\Psi_{\sigma,anom}$ in both experiments, an approximate 5 year lag in time between the onset of additional surface forcing and the increase in flow rate out of the region is observed. What is notable when considering the adjustment in denity space is how the adjustment occurs at lower densities ($\sigma \simeq 1.0$ kg/m^3) than the densities of the strongest surface water mass transformation ($\sigma \simeq 1.1 - 1.2$ kg/m^3). The change in MOC is also distributed over a larger band of density layers, whereas the change in F is consantrated over a very narrow band of potential densities. This suggests diapycnal mixing of the water masses after the initial surface transformation plays an important role in how the altered water contributes to the MOC. This means that the dense water masses formed at the surface do not simply mix down vertically to their neutral density layers, to then spread and feed into the MOC along the corresponding isopycnal. The apparent contribution from diapycnal mixing is possibly linked to the predicted *lateral exchange and spreading*-phase. Note also how *Open [EKE]* seems to spread over a slighly wider range of density layers than *Open [std]*. This suggests that the representation of meso-scale eddies play a role in how the MOC adjusts to the localized forcing, even if the difference is not large enough to say something definitive.

It is also notable that in both *Open [std.]* and *Open [EKE]*, the magnitudes of the MOC adjustment is significantly smaller than the magnitude of the surface transformation. The difference in magnitudes between the terms suggest that some of the transformed water likely resides within the northern region over longer times than the time scale of the initial MOC adjustment. One caveat to these results is that the densest water formed at the surface during the experiment ($\sigma \geq 1.1$ kg/m^3) does not share any isopycnals out of the northern region at the initial time of the experiment. Since there are no isopycnals out of the region for the densest water masses formed at the surface, the net change in overturning out the region must happen along less dense isopycnals. This is a consequence of how the experiment is set up, and does not necessarily represent conditions in the real ocean.

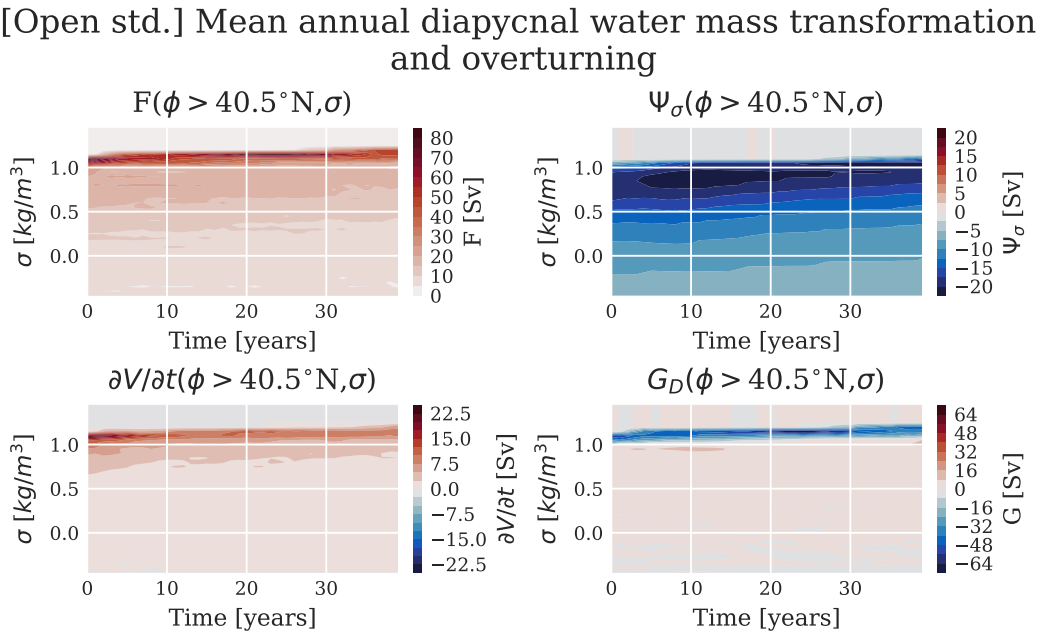

(a)

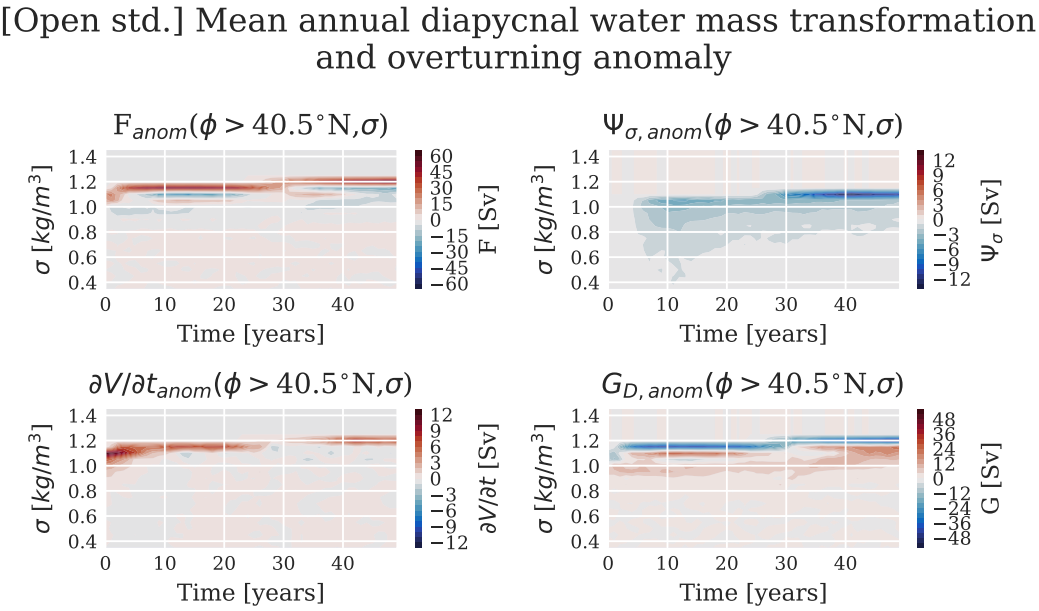

(b)

Figure 4.14.: (a) *Open [std.]*: Mean annual contributions of each term in (2.35) to the volume and buoyancy-budget of the region north of $40.5°$N, for a given density level σ. Spacing between each density levels is $\Delta\sigma = 0.05$ kg/m^3. Time is in years after onset of localized forcing. Note different scales for different terms. Note also that the full range of reference density levels ($\sigma = [-4, 1.5]$ kg/m^3) is not displayed, but has been cropped to emphasize the most relevant patterns. (b) Same as in (a), but showing now the difference between the value of each term and the corresponding values of *Ctrl [std.]*. Note also that a smaller density range is displayed than in (a).

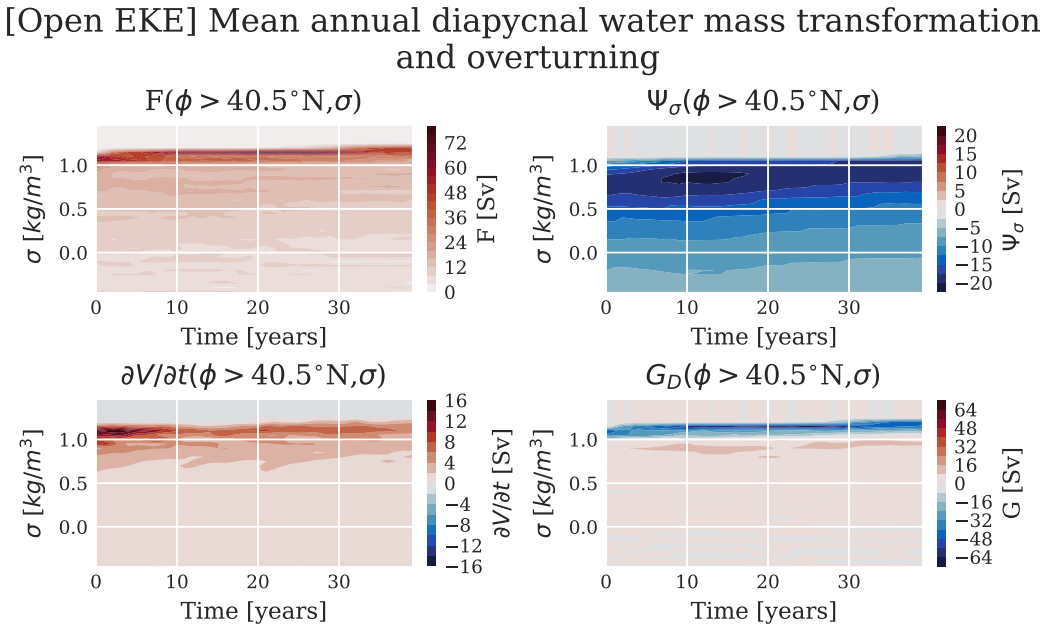

(a)

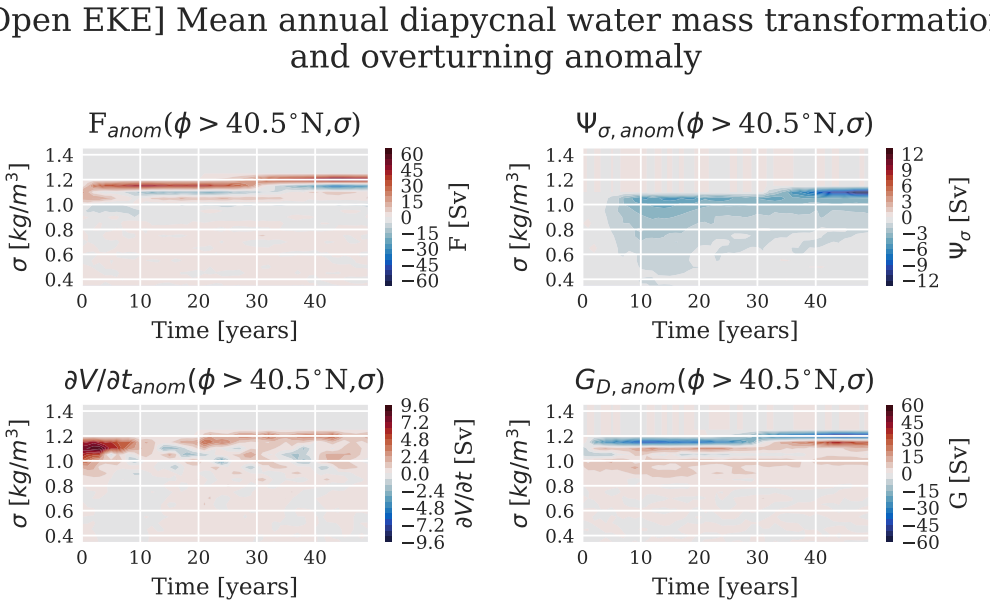

(b)

Figure 4.15.: (a) *Open [EKE]*: Mean annual contributions of each term in (2.35) to the volume and buoyancy-budget of the region north of $40.5°$N, for a given potential density level σ. Spacing between each density levels is $\Delta\sigma = 0.05$ kg/m^3. Time is in years after onset of localized forcing. Note different scales for different terms. Note also that the full range of reference density levels ($\sigma = [-4, 1.5]$ kg/m^3) is not displayed, but has been cropped to emphasize the most relevant patterns. (b) Same as in (a), but showing now the difference between the value of each term and the corresponding values of *Ctrl [EKE]*. Note also that a smaller density range is displayed than in (a).

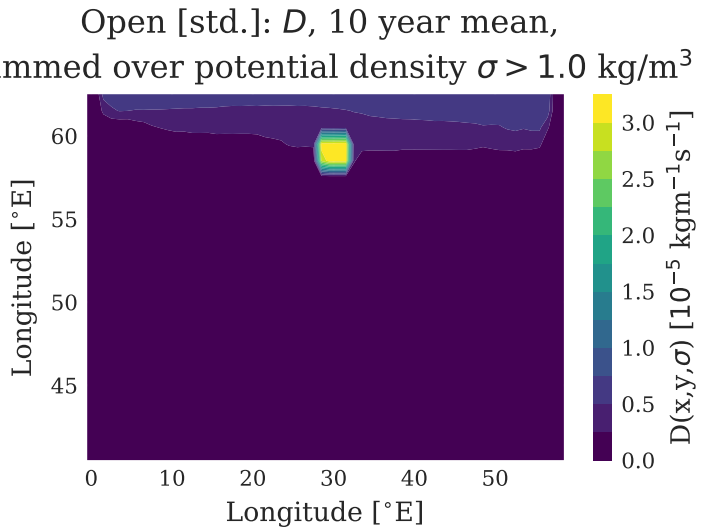

Figure 4.16.: *Open [std.]:* Spacial distribution of the local rate of surface water-mass transformation D, averaged over the first 10 years of experiment time, summed over all $\sigma > 1.0$ kg/m^3.

To confirm that the densest water masses are indeed formed over the region of open-ocean convection, Figure 4.16 shows the spatial distribution of the local rate of surface-forced water mass transformation D, as defined in (2.37), summed over all density layer $\sigma > 1.0$ kg/m^3 averaged over the first 10 years of *Open [std.]*. While some water is transformed near the northern boundary, it is clear that the strongest transformation occurs over the mixed patch. This corresponds to what is seen in Figure 4.3, where isopycnals connect dense deep waters to the surface of the mixed patch.

A final remark about the way in which the Walin-framework is calculated here, is how closing the budget by assigning the residual from the other terms to G_D does not distinguish between contributions from actual diapycnal mixing and contributions from numerical noise. While an important question, attempting to estimate how much of the residual is due to numerical errors is outside of the scope of this thesis.

4.4 Large-scale adjustment in depth space

Figure 4.17a shows the deviance of the MOC strength at $15°$ of the four low-resolution experiments from their corresponding control run. Figure 4.17b shows the corresponding change in surface buoyancy flux due to the localized forcing, with negative values indicating stronger forcing. Note that time in both figures is relative to the onset of the localized forcing, not the

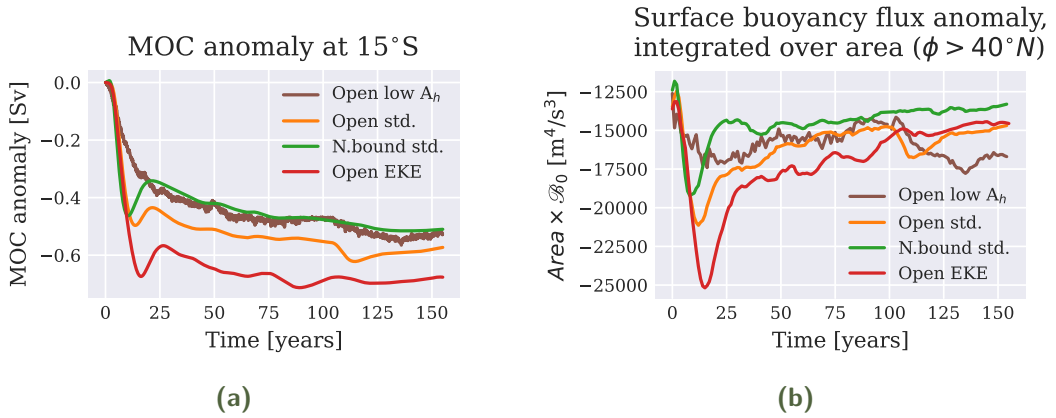

Figure 4.17.: (a) Time series of annual mean MOC strength anomaly relative to the unforced control-run ($\Psi_{max,exp}(\phi,t) - \Psi_{max,ctrl}(\phi,t)$), evaluated at 15°S. More negative values indicate stronger MOC anomaly. Time is in years after onset of localized forcing. (b) Time series of the annual mean additional (forced experiment minus corresponding control) surface buoyancy flux north of 40°N, integrated over the area. Time is in years after onset of localized forcing. Negative buoyancy fluxes correspond to an increase in total buoyancy forcing.

initialization of the spin-up. The adjustment timescales of the MOC strength show similar general patterns, with a strong response through the first 10 to 20 years, followed by a slight adjustment before stabilizing in a state of gradual in strengthening after 20 to 25 years. The exception is *Open [low A_h]*, which shows a smoother adjustment, albeit still reaching a quasi-steady state within the same timeframe.

The timescales of the MOC adjustment largely correspond with the patterns of the surface buoyancy flux, where an extremum is reached within the first 10 to 20 years before adjusting and stabilizing after roughly 20 to 25 years. As with the MOC anomaly, the surface buoancy flux in *Open [low A_h]* is the exception to this pattern. The relative magnitudes of the MOC responses also largely correspond with the magnitudes of the added buoyancy fluxes, where *Open [EKE]* shows the largest change, the response of *Open [std.]* is slightly stronger than *N.bound [std.]*, which after initial adjustment shows similar values to *Open [low A_h]*.

The surface buoyancy flux is a function of the difference in salinity and temperature to the enforced surface reference values. Since *Open [EKE]* has a slightly larger $S_{surf,init}$ than *Open [std.]*, as given in Table 3.2, and they are forced with the same S_f, one might think that part of the difference in surface buoyancy flux is likely to be caused by a difference in how rapidly added salt

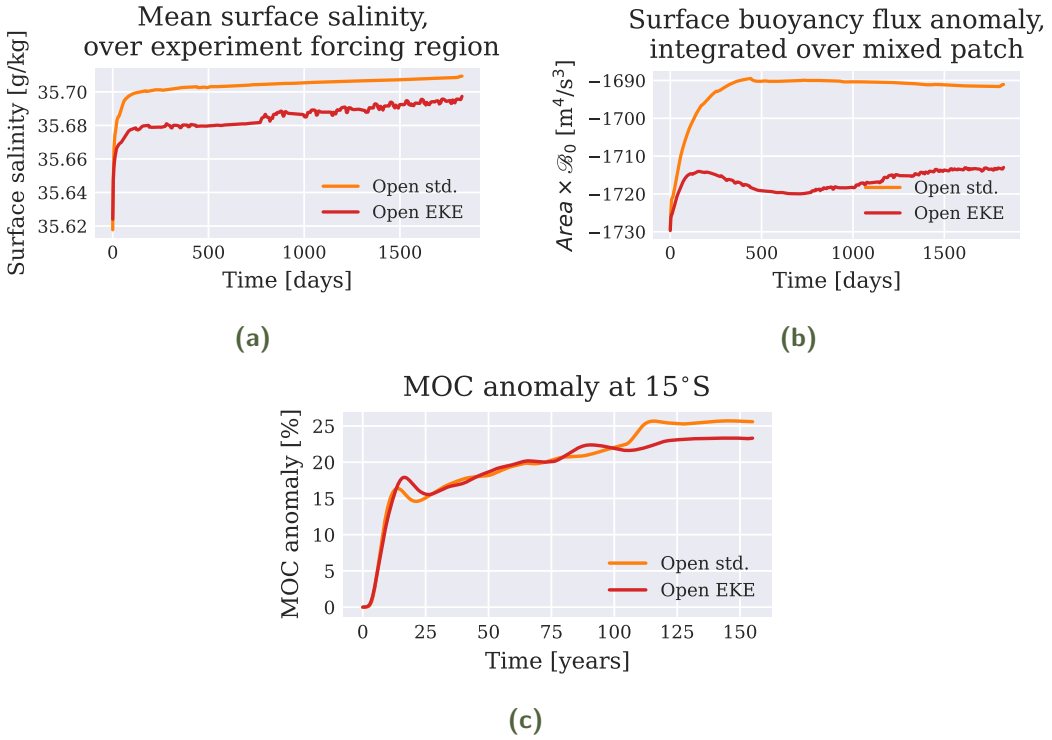

Figure 4.18.: *Open [std.] & Open [EKE]*: (a) Five year time series of daily mean surface salinity over the *Open* forcing area. Time is in days after onset of localized forcing. (b) Five year time series of additional (forced experiment minus corresponding control) surface buoyancy flux integrated over the *Open* forcing area. Time is in days after onset of localized forcing. Negative buoyancy fluxes correspond to an increase in total buoyancy forcing. (c) Time series of the percentage wise MOC adjustment ($100 \times (\Psi_{max,exp}(\phi,t) - \Psi_{max,ctrl}(\phi,t))/\Psi_{max,ctrl}(\phi,t))$), evaluated at $15°$S. Time is in years after onset of localized forcing.

is transported away from the surface of the forcing region. This is supported by the results in Figure 4.18a & 4.18b, which give a more detailed view of the surface salinity and buoyancy fluxes of *Open [std.] & Open [EKE]* over the first five years after the forcing is initiated. The latter stabilizes at a lower surface salinity, causing the persistence of a stronger surface buoyancy flux anomaly. It is a reasonable conclusion that the surface salinity stabilizes when the salinity transport away from the surface is equal to the surface salinity flux over the region, which confirms that the salinity is more efficiently mixed away in *Open [EKE]*. It is not clear if this is due to more efficient lateral eddy transport, a consequence of the deeper initial mixed layer, or because of differences in background circulation.

Note however that the observed difference in $\mathscr{B}_0$ anomaly over the mixed patch between *Open [std.]* and *Open [EKE]* is marginal compared to the difference in Figure 4.17b. Rather, it seems that the bulk of the difference must be explained by surface processes over the area north of $40°$ surrounding the mixed patch. Here, it is more challenging to isolate the differences between the two configurations, as they have different surface temperature- and salinity profiles at the initiation of the experiments, and these respond differently to the forcing and the adjustments of the circulation patterns. On this note, as shown in 4.2, the initial MOC strength in the *EKE* configuration is already stronger than *std.*. To control for this, Figure 4.18c shows the percentage wise adjustment of the MOC strength at $15°$ for *Open [std.]* and *Open [EKE]*, relative to their respective control runs. Here, it is evident that when controlling for the initial differences between the two configurations, the details of the difference near the mixed patch seem to be negligible in the long-term large-scale response.

Differences in how efficient salt is transported away from the surface may also play a role in the difference between *Open [std.]* and *N.bound [std.]*. This would agree with the pattern found in 4.2, where *N.bound [std.]* exhibits less lateral mixing than the other configurations. However, in this case, we must also consider the larger $S_{surf,init}$ of *N.bound* which reduces the initial strength of the salinity forcing, the somewhat smaller forcing area of *N.bound* due to the curvature of the Earth, and different background surface circulation of the two regions, resulting in different responses of the surrounding areas to the salinity forcing.

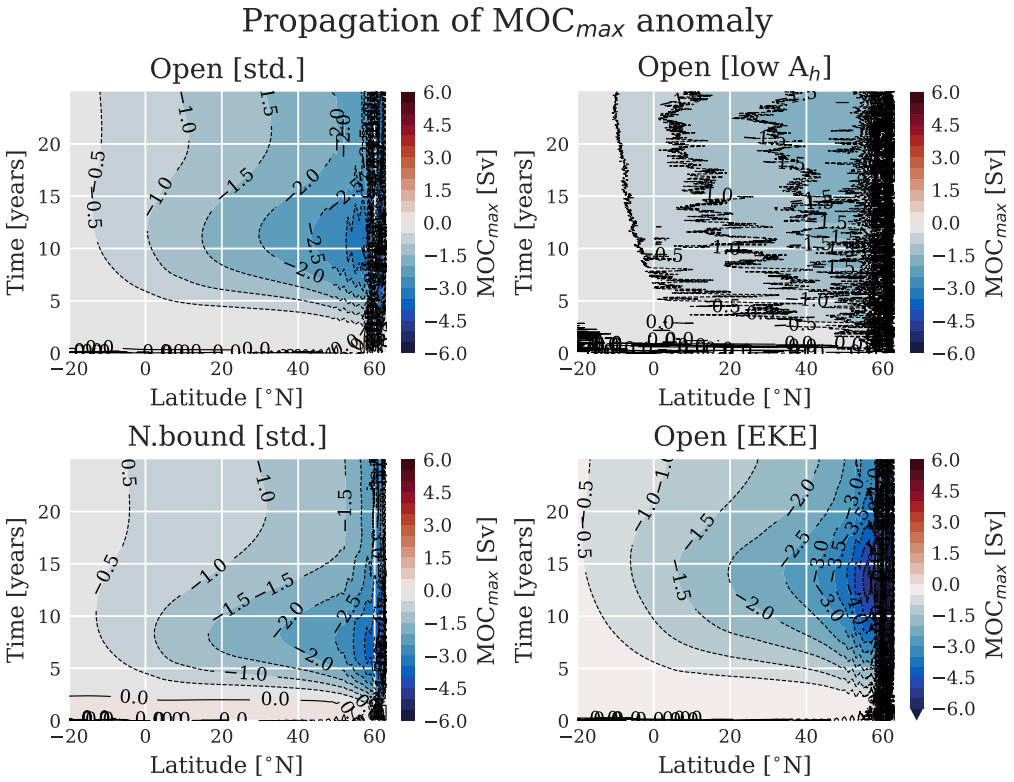

(a)

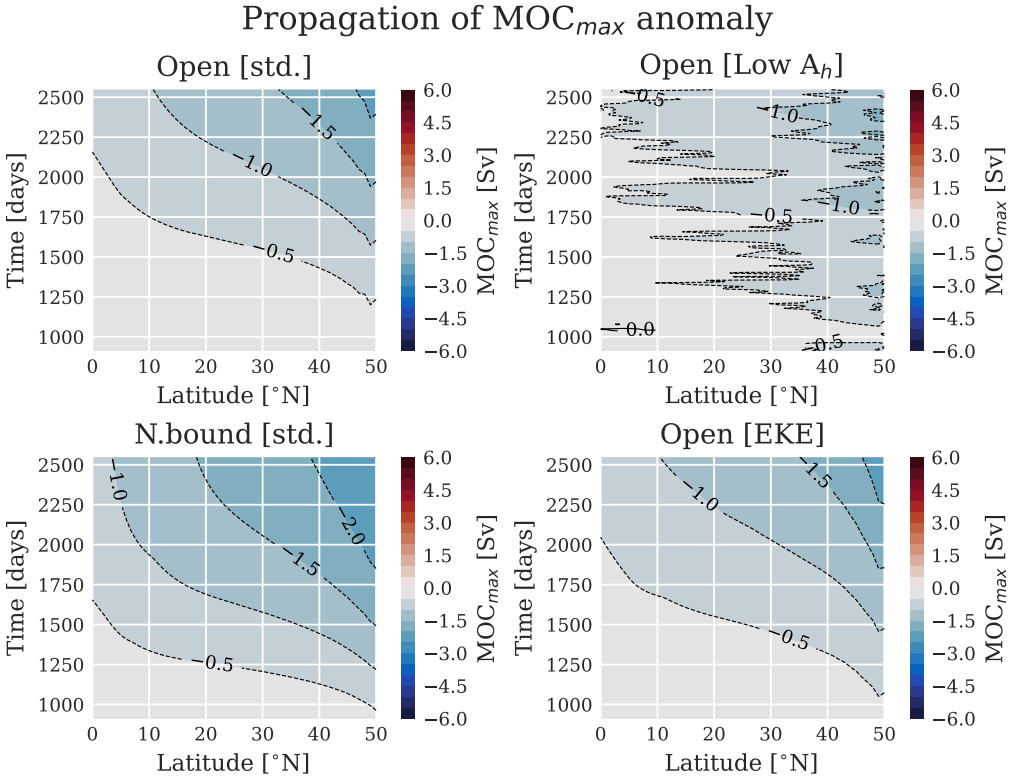

(b)

Figure 4.19.: Southward propagation of MOC anomalies ($\Psi_{max,exp.}(\phi,t) - \Psi_{max,ctrl}(\phi,t)$). More negative values indicate stronger overturning. (a) Adjustment over first 25 years after localized forcing is initiated. (b) Adjustment from 1000 to 2500 days after localized forcing is initiated.

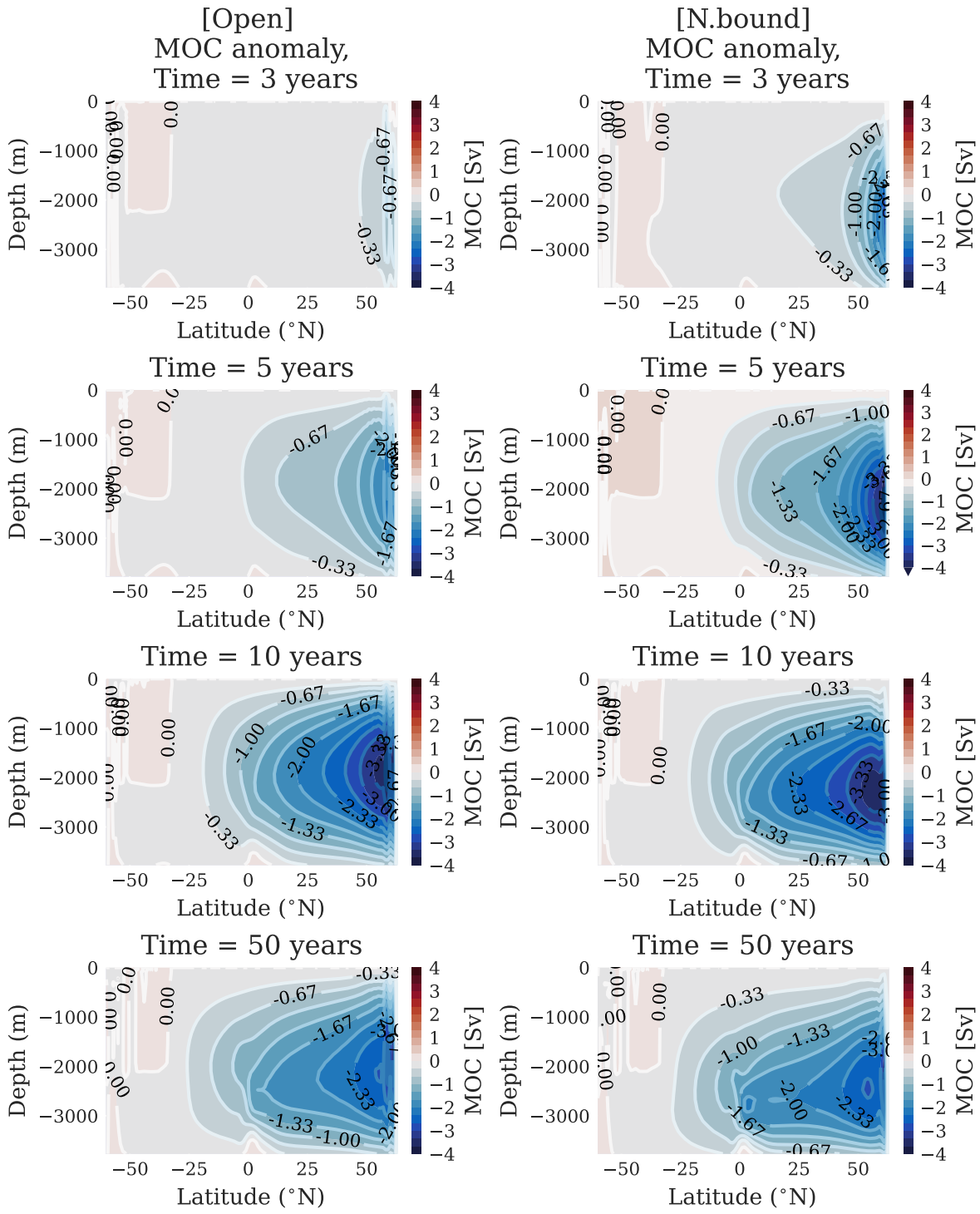

Figure 4.20.: *Open [std.] & N.bound [std.]*: Snapshots of MOC response to localized surface salinity forcing at high latitudes. Shows anomalies ($\Psi_{exp}(\phi, z, t) - \Psi_{ctrl}(\phi, z, t)$) in vertical streamfunction at 3 years, 5 years, 10 years and 50 years after localized forcing is initiated in either the open ocean or at the northern boundary.

A more detailed view of how MOC anomalies caused by the localized forcing propagate southwards can be gained by considering how the MOC strength at a given latitude changes in time, as shown in Figure 4.19a. Here we see more clearly that although the large-scale patterns of adjustment are overall similar, there are some notable differences. When the forcing is located at the northern boundary, the initial response is slightly more rapid, reaching the equator in less than five years. Likewise, the anomaly maximas at each latitude are also reached sooner. The adjustment of *Open [std.]* is slower but stronger, taking just above five years to reach the equator, and reaching its peak right after a decade. The subsequent decline following the peak is also not as strong, maintaining a stronger permanent change to the MOC strength at distance from the forcing region. *Open [EKE]* also takes just over five years to reach the equator, and reaches its peak just before 15 years. As also seen in Figure 4.17a, the response here is even stronger than in *Open [std.]*.

In each of the three cases discussed above, it seems that lag in initial adjustment mostly originates north $40°$N, and the signal propagates very rapidly from $40°$N to $10°$N. It seems to take 2-3 year before the signal even begins propagating at all, slightly shorter for *N.bound*, which is likely explained by the time it takes for the signal to reach the western boundary in the first place. Figure 4.19b shows a more detailed view of the initial respons. The signals propagate from $40°$N to $10°$N in 200-400 days, giving average velocities ranging from ~ 9 cm/s to ~ 19 cm/s.

Open [low A_h] is again the experiment that most notably differs from the patterns seen in the other experiment. Although it is partly obfuscated by noise, we note again that the response lacks the clear maxima and subsequent reducation that can be seen in the other cases, showing instead a more steady response.

So far, we have only considered the strongest anomaly at any latitude, but it is also interesting to consider how the full overturning adjusts at depth. Figure 4.20 compares the response of *Open [std.]* and *N.bound [std.]* at select times following the onset of localized forcing, showing the difference between the forced runs and the control-run. First to note, this figure makes the initial difference in response time between the *Open* and the *N.bound* forcings very evident, where the response is stronger to forcing at the northern boundary within the first 5 years. By 10 years however, the difference has nearly vanished. It is further interesting to compare the anomalies to the unperturbed states

in Figure 4.1. The MOC anomalies in both cases initially appear strongest around 2000 meters depths, before they seem to gradually deepen over time. Compared to the unperturbed state, which is at its strongest above 2000 meters, it is clear that the additional forcing effectively deepens the overturning cell.

4.5 Velocity field and deep water distribution

The overturning stream function in depth- and density space can only give information about the zonal mean of the circulation, and important details about the full three dimensional structure of the overturning are lost. Figure 4.21 shows the horizontal velocity field at select isopycnals $\sigma = 1.0$ kg/m^3 and $\sigma = 1.1$ kg/m^3, chosen based on the levels of strongest MOC adjustment shown in 4.14b, for *Open [std.]*. Contours show the depth of the respective isopycnals. Looking at the velocity field and isopycnal depth at select times after the onset of the localized forcing, the structure of the circulation exhibits the expected pattern of a strong WBC in the northern hemisphere, turning eastwards near the equator. Looking at the depth of the isopycnals in Figure 4.21a, it is also clear how in this setup, deep water is asymmetrically formed in the north and south, with stronger formation in the north. The water masses formed in the north then spread southwards along the western boundary and eastwards at the equator. Notably, the deep water seems to be distributed within the region between the western boundary and $30°$E of the northern hemisphere well before they are distributed accross the equator. This is even more clear when looking at Figure 4.21b. It is evident that the water masses of density $\sigma = 1.1$ kg/m^3 formed during the convection are denser than all other water masses distributed through the ocean, and so we can clearly follow how the dense water spreads from the northern region, and crucially, has not crossed the equator yet within the first 60 years after the formation, but is already filling up the abyss of the northwestern region of the domain.

4.6 Signal propagation

Based on the velocity field and spreading of dense water show in Figure 4.21, it seems that the most relevant signals propagate along the northern and western boundary. To measure the velocity of a signal propagating along the boundaries, I trace buoyancy anomaly contour lines along the depth layer at 2190 m. This depth is chosen based on approximately where the overturning anomaly seems strongest, as indicated by Figure 4.20. This

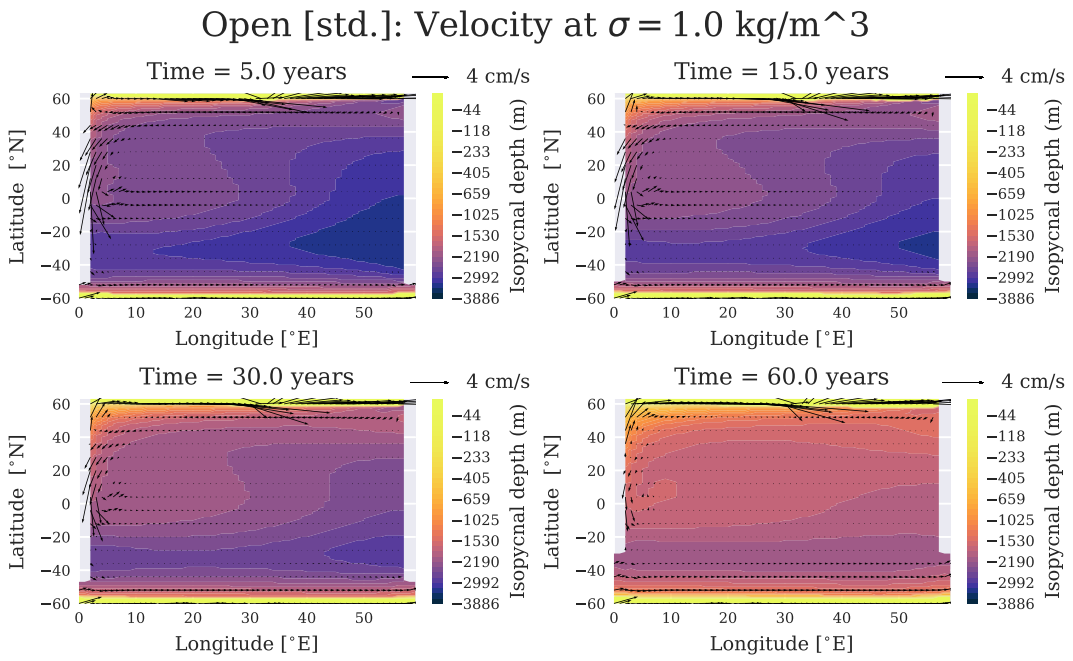

(a)

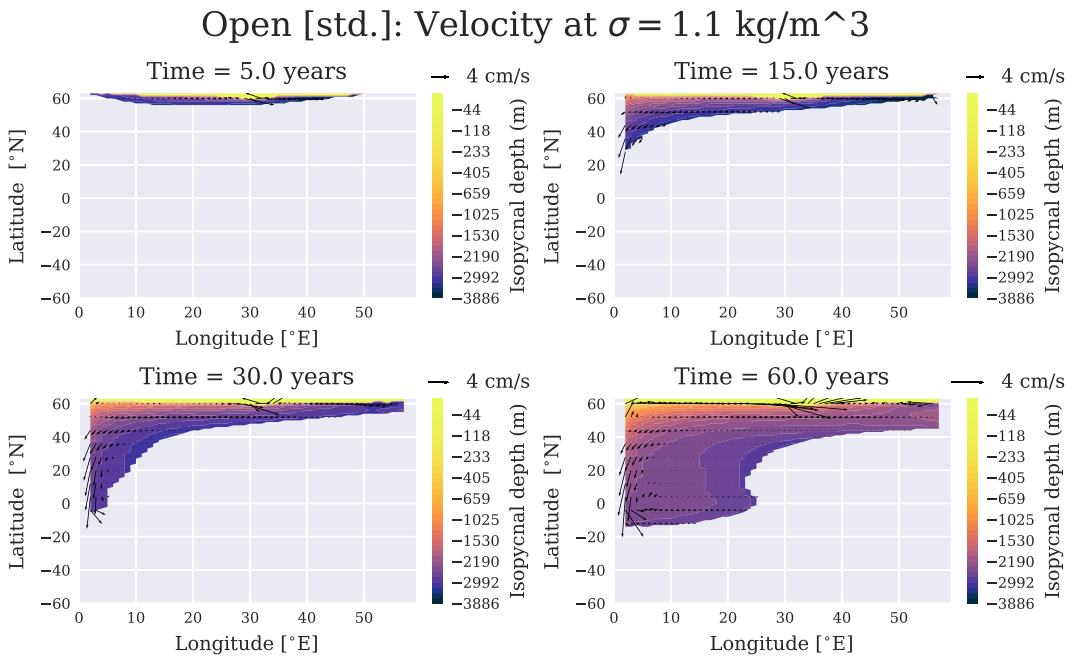

(b)

Figure 4.21.: Horizontal velocity field at given isopycnals, along with depth of the respective isopycnal layers, at a given time in years after localized forcing is initiated. Quivers show velocity field (note varying scale as indicated by reference arrow in top right corner), contours show depth of the isopycnal. (a) Velocity and depth of isopycnal $\sigma = 1.0$ kg/m^3. (b) Velocity and depth of isopycnal $\sigma = 1.1$ kg/m^3. Note that lack of data indicates that water of that density does not yet exist for those coordinates, illustrating how the water masses of the given density is produced in the north and then spreads. Time is in years after onset of the localized forcing.

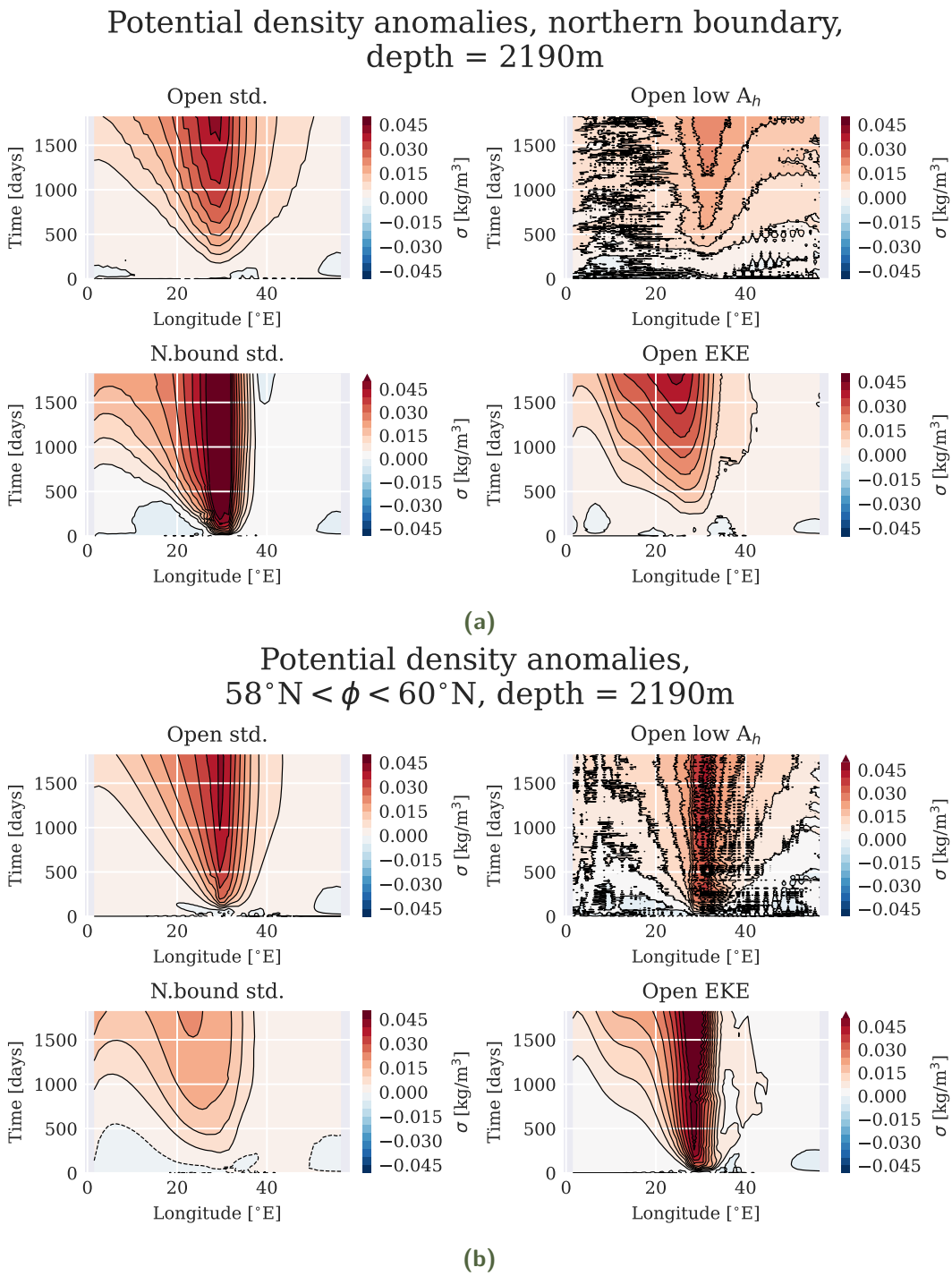

Figure 4.22.: Signal propagation along (a) northern boundary, and (b) the latitude bands of the open ocean forcing, as given by potential density anomalies (deviance of experiment from corresponding control-run), all 1° experiments. Depth 2190 m is approximately where the AMOC response appears to be strongest, as shown in Figure 4.20. Time is in days after onset of localized forcing.

method of measuring signal propagation timescales is common, but is flawed in that it does not account for changes in propagation amplitudes along the path (see Marshall and Johnson (2013) for a discussion on this). It should also be noted that propagating signals are often measured near the pycnocline as this is where first-mode baroclinic waves are expected to propagate, and this is typically at depths shallower than 2190 meters (Marshall and Johnson, 2013). Several other depth layers have been tested besides the ones shown here, both shallower and deeper, without significant differences to the signal propagation.

Figure 4.22a shows the signal propagation along the northern boundary for the first five years following the experiment start, for the four low resolution experiments. Figure 4.22b shows the same, but this time over the latitude bands of the open-ocean forcing ($58°$N$< \phi < 60°$N). For each experiment, we clearly see a signal originating at the longitudes of the localized forcing. For the experiments in open ocean, we can also see the time it takes for the signal to move from the region of the forcing to the northern boundary, which for *Open [std.]* and *Open [EKE]* takes about 250 days. Despite the time it takes takes for the signal to reach the northern boundary, the signals measured at the northernmost latitudes still reach the western boundary sooner than the signals propagating at the latitude bands of the open ocean forcing. For *Open [low A_h]* it is harder to distinguish due to noise, but the same pattern can be seen.

Considering the fastest propagating signal for *Open [std.]* along the northern boundary, it propagates with a near constant velocity and covers a longitudinal distance of $20°$ in roughly 800 days, giving a propagation velocity of ~ 1.5 cm/s. *Open [EKE]* has a less linear propagation along the boundary. The signal is initially faster, crossing the distance from $30°$E to $10°$E in roughly 350 days, corresponding to an average velocity of ~ 3.5 cm/s. The signal slows down as it nears the boundary, but still arrives at the western edge sooner than *Open [std.]*. The signal from *N.bound [std.]* reaches the western boundary first, seemingly owing to the fact that the signal already originates at the boundary. The velocities from $30°$E to $10°$E are similar to the velocities of *Open [std.]*, but the signal seems to speed up as it nears the boundary. This is possibly due to sloping isopycnals and impact from signals propagating at different depth levels. For reference, the mean zonal velocity at the given depth level along the northern boundary, between $10°$E and $30°$E, averaged over the five year period after the forcing is iniated, is found to be $u \simeq -0.5$ cm/s for *Open*

[std.], and $u \simeq -0.3$ cm/s for *Open [EKE]*. Negative values here means that the velocity is westwards. This suggests that the propagation along the boundary is not by advection, leaving some form of boundary waves as the most likely explanation.

In Figure 4.23, signals along the western boundary are examined at three different timescales, compared between *Open [std.]* and *Open [low A_h]*. I choose to highlight these because *N.bound [std.]* and *Open [EKE]* show very similar propagation to *Open [std.]* along the western boundary. On the shortest timescale, shown in the upper row, it is clear how the lower viscosity allows for rapid signals that are dampened out in the higher viscosity case. Whereas there are no distinguishable patterns within the first 100 days ofter the forcing is initiated in *Open [std.]*, *Open [low A_h]* shows rapid buoyancy signals propagating across the northern basin within $1-2$ months. This corresponds to velocities of ~ 1.5 m/s, which is consistent with typical Kelvin wave velocities. Note however the small amplitude of the variation. A more complex interplay of signal propagation at different timescales and amplitudes could help explain the adjustment pattern of *Open [low A_h]* seen in Figure 4.17a, where the distinct strong response followed by slight re-adjustment prevalent in the standard viscosity configurations is absent.

The second row shows intermediate timescales, showing an interval from 800 to 1500 days after localized forcing is initiated. Whereas *Open [low A_h]* shows no distinct signals at this timescale, *Open [std.]* clearly shows signals propagating southwards. The time it takes the initial signal to propagate from $40°$N to $10°$N is around 400 days, corresponding to velocities of ~ 9 cm/s, similar to what was found for the initial MOC response in 4.17a. The behaviour north of $40°$N and south of $10°$N is possibly due to sloping isopycnals in the region of uniform salinity forcing as well as near the equator.

Finally, the third row shows interdecadal timescales. For both *Open [std.]* and *Open [low A_h]*, strong but slow signals reach the equator on the order of a decade. The velocity seems to increase south of $20°$N, more so for *Open [low A_h]*. For *Open [std.]*, following the first contour, the average velocity of the signal across the northern basin is ~ 2 cm/s.

Where the signal propagating at 9 cm/s seems to correspond to timescales of the initial response of the overturning circulation, the timescales of the stronger decadal signals seem to correspond to the timescales of adjustment towards equilibrium of the overturning. For reference, the mean meridional

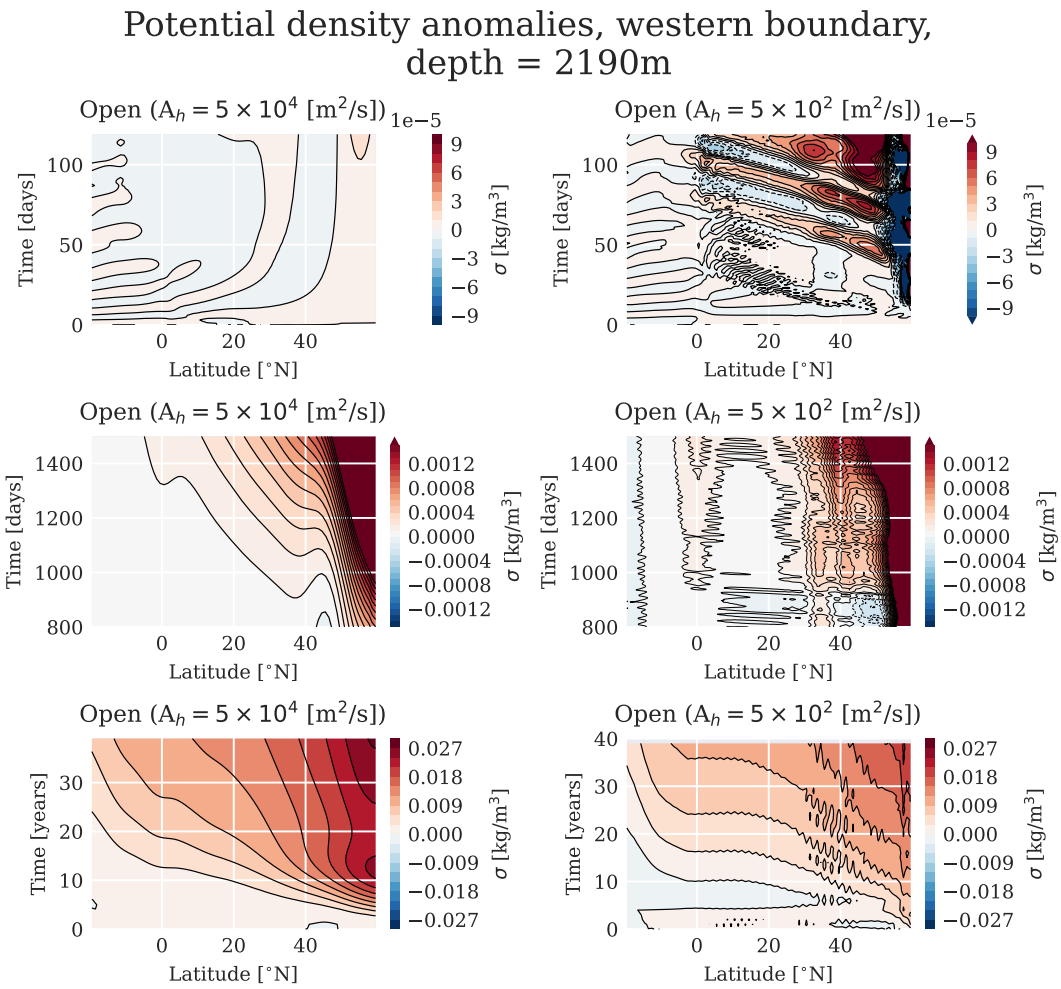

Figure 4.23.: Signal propagation along western boundary at different timescales, as given by potential density anomalies (deviance of experiment from corresponding control-run), comparison between *Open [std.]* (left) and *Open [low A_h]* (right). Depth 2190 m is approximately where the AMOC response appears to be strongest, as shown in Figure 4.20. Time is in days and years after onset of localized forcing. Note different scales for the anomalies at different timescales.

velocity at the given depth level along the northern western, between the equator and $40°$N, averaged over a 10 year period after the forcing is iniated, is found to be $v \simeq -4$ cm/s for *Open [std.]* Negative values here means that the velocity is southward. This suggests that the initial response of the MOC is not likely to be communicated by advection. It is on the other hand likely that the slower, stronger signal is advective, and dominates as the adjustment approaches steady state.

4.7 Upwelling

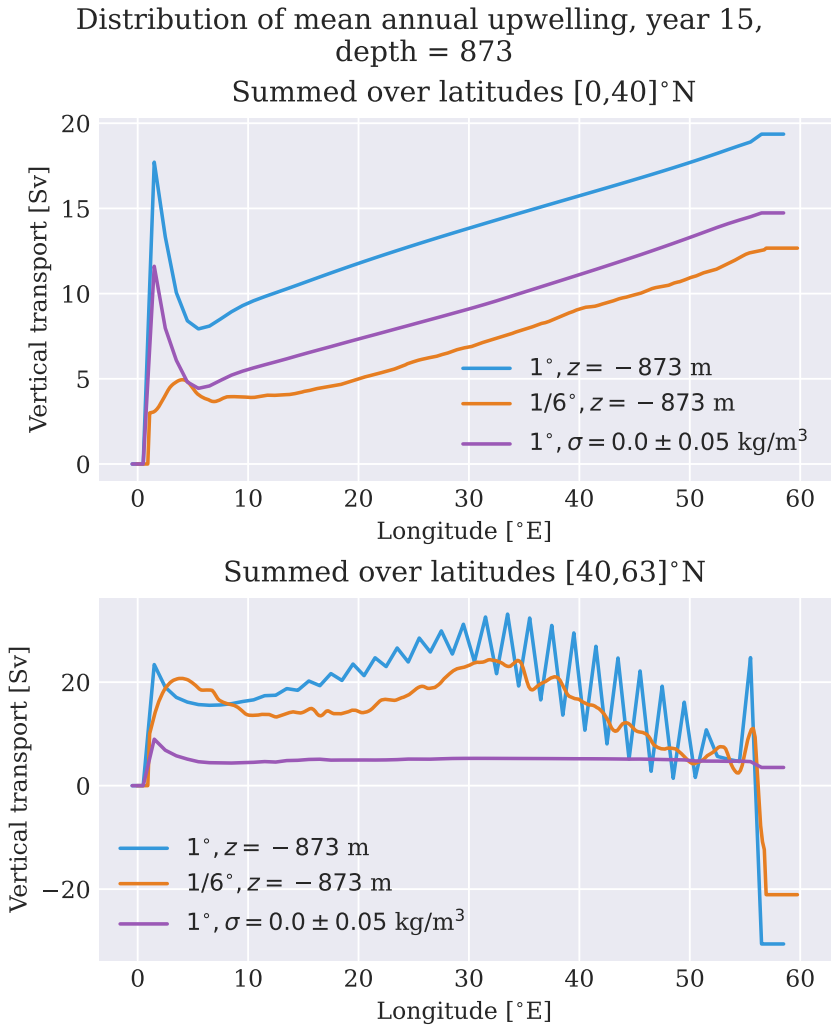

Figure 4.24.: [*std.*& *HR*] Cumulative sum of upwelling from western to eastern boundary, after 15 years of spin-up, comparison of $1°$ at depth 873 meters (blue), $1/6°$ at depth 873 meters (orange), and $1°$ along isopycnal $\sigma = 0.0 \pm 0.05$ kg/m^3 (purple). Top figure shows the region from the equator and to $40°$N, bottom figure shows the region of uniform salinity forcing north of $40°$N

Finally, a brief look at the upwelling that closes the loop. Figure 4.24 shows a comparison of upwelling north of the equator in the standard low-resolution configuration and the high-resolution configuration. Both configurations are considered at year 15 of the spin-up. Since different patterns of upwelling are expected north and south of $40°$N, due to the uniform salinity forcing in the northern region, the two sections are considered separately. The upwelling across the layer at depth 873 meters is calculated as the vertical velocity times the area of each grid cell. The figure shows the cumulative sum, taken from the western to the eastern boundary, summed first over the respective latitude ranges of the section. In the $1°$ configuration, the upwelling along the westernmost grid cells in the section south of $40°$N is stronger than the upwelling of the entire interior at those latitudes. There is also a strong downwelling in the neighboring grid cells, compensating for some of the strong upwelling.

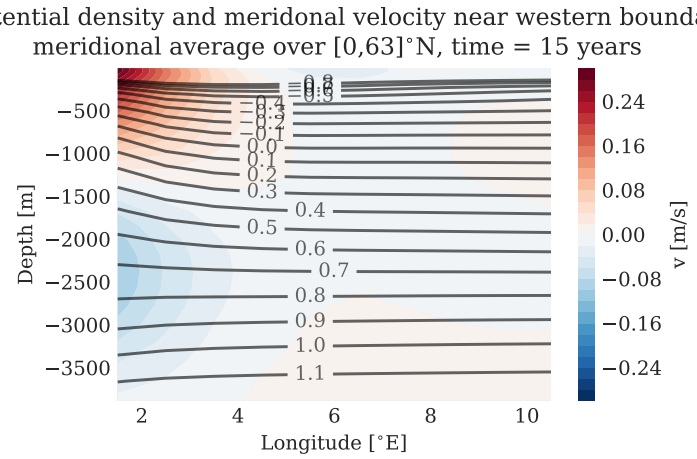

Figure 4.25.: Annual mean meridional velocity v (filled contours) and potential density σ (contour lines), averaged over the northern hemisphere, at year 15 of spin-up.

The high-resolution model also shows upwelling in the first cells along the western boundary. In fact, vertical velocities there are even larger than in the low-resolution model. However, since the area of the cells is much smaller in the $1/6°$ resolution, the total upwelling is not as large. As a result, the high-resolution model does not exhibit the same dominance of the western boundary in terms of upwelling, but instead sees most of the upwelling happen in the interior.

From Figure 4.25, we see that isopycnals the selected depth of $z = -873$ m slope slightly upwards. This raises the question of whether the upwelling

seen at the western boundary is predominantly diapycnal, or along the sloped isopycnals. The purple lines in Figure 4.24 show the upwelling in density space at potential density $\sigma = 0.0$ kg/m^3, approximately corresponding to the 873 meter depth-layer, for the 1° configuration. While the same pattern of upwelling at the western boundary and compensating downwelling next to it persists, the magnitude is reduced. North of 40°, the selected isopycnal crops out in most of the region, explaining why there is no change across the interior. Note also the grid-scale noise for the low-resolution model in the northern region, as well as the strong downwelling at the eastern boundary.

Discussion and conclusion 5

5.1 Summary and comparison with theory and previous results

5.1.1 Open-ocean convection in Veros

In this thesis, I set out with the goal of exploring how small-scale processes of open-ocean convection and the large-scale MOC are connected. The first step was to examine whether the localized surface buoyancy flux enforced in each experiment lead to a local response resembling theoretical and observational descriptions of open-ocean convection in the first place. Taking into account that key processes of open-ocean convection occur at sub-grid scales, the *Open* 1° configurations seem to largely capture the bulk properties expected of the mixed patches as described in section 2.2. In each case, steep isopycnals form surrounding the patch, and surface properties such as salinity initially mix vertically akin to the *deep convection*-phase, before eventually spreading laterally. Vertical velocities across the patch are at their largest on the order of ~ 0.01 cm, meaning they are close to neglible, as predicted by the theory presented in 2.2.3.

The vertical mixing timescale t_{mix} appears to be larger than what is predicted by (2.22), which suggests mixing to the base of the mixed layer in less than a day with the given Ro^* and $f \sim 10^{-4}$ s^{-1}. In the experiments, surface properties seem to take more than 10 days to mix down to the initial MLD. However, I do not expect that differences in mixing timescale on these orders should play any significant role in the context of large-scale adjustment.

As for the scaling relation for the MLD quasi-equilibrium, the estimated constants of proportionality $\gamma_{std.} = 2.4 \pm 0.2$ and $\gamma_{EKE} = 2.3 \pm 0.2$ place the 1° results between the $\gamma_{Sohail} = 1.76$ found using a turbulence resolving model, and $\gamma_{Visbeck} = 3.9 \pm 0.9$ found by a combination of experimental results and model results. For the $1/6^\circ$ configuration, $\gamma_{HR} = 7.8 \pm 0.5$, suggesting that the mixed layer deepening is less effectively constrained lateral eddy transport in the eddy-permitting model. This could be a sign that the parameterization

used in the non eddy-permitting models overestimate the eddy transfer. However, as the $1/6^\circ$ is not fully eddy resolving and *Open [HR]* still implements the same mesoscale eddy closure as *Open [std.]*, only with lowered diffusivities, it is not necessarily given that the baroclinic eddy transfer efficiency is more realistic in this configuration than in the 1° models. An interesting extension of these results would be to test how different magnitudes of K_{iso} and K_{gm} impacts γ.

The constant of proportionality for the equilibrium timescales t_{equil} of the MLD $\beta_{EKE} = 14 \pm 22$ and $\beta_{HR} = 13 \pm 20$ fall well within the range of $\beta_{Visbeck} = 12 \pm 3$ Even $\beta_{std.} = -11 \pm 23$ shows overlapping uncertainty ranges with $\beta_{Visbeck}$ (admittedly due to the very large standard errors). Regardless, as indicated by the large standard errors, t_{equil} does not follow the predicted scaling relation as closesly as h_{equil}.

Finally, the eddy-permitting configurations seems to capture the predicted pattern of rim-currents surrounding the patch forming due to the thermal wind-balance, that over time begin to meander and shed off eddies, exchanging buoyancy between the mixed patch and its surroundings.

As a summarizing remark on the overall short-term local response to the enforced buoyancy flux, it seems within reason to conclude that Veros is able to reproduce the expected mixed patch dynamics to a satisfying degree as pertains to the goals of this thesis, even in the coarse resolution configurations. With this in mind, it is time to return to the four questions put forward in the introduction.

5.1.2 First research question

Does surface-forced convection adjacent to a vertical boundary result in significantly different large-scale AMOC adjustment than convection in open ocean? The short answer is no. The local adjustment in *N.bound [std.]* is certainly different from *Open [std.]*, with stronger vertical velocities over the mixed patch (albeit still small), mixing down to the abyss over shorter timescales, and less mixing in lateral directions except along the ocean bottom. The initial response of the AMOC is slightly faster, likely because the signal from the mixed patch to the western boundary is predominantly communicated along the northern boundary, meaning the main difference is in the time it takes the signal to travel from the *Open* region to the northern boundary. Over longer timescales, this difference is virtually negligible. Differences in

magnitude between the two is likely due to how the experiments is conducted. *Open [std.]* and *N.bound [std.]* are forced using the same S_f, but due to differences in forcing area, initial surface salinity and background currents of the two regions, the enforced buoyancy flux is weaker over time at the northern boundary. However, differences in efficiency of transport of salinity away from the forcing region may also be a factor, and this may be tied to the different dynamics of convection adjacent to vertical boundaries. I have not been able to determine with certainty the possible reason for the difference in magnitude of the adjustments. Nevertheless, while it can not be ruled out that differences in dynamics of the two regions contribute to the difference in magnitude, the overall results indicate that whether the convection is adjacent to a vertical boundary or not does not play a major role when concerned with long-term AMOC adjustments. One aspect not examined here, but which could be worth investigating, is whether the structure of the abyssal waters differs in the two cases, since the forcing at the northern boundary seems to spread at depths to a greater degree than what is the case for the forcing in open ocean.

5.1.3 Second research question

How will the local processes of open-ocean convection and the subsequent large-scale adjustment differ if meso-scale eddy diffusivities are determined prognostically with spatial variation, as opposed to being given by pre-set constant parameters? This was tested by utilizing the prognostic EKE closure by Eden and Greatbatch (2008), compared to the standard configuration with constant eddy diffusivities $K_{iso} = 1000$ m^2/s and $K_{gm} = 1300$ m^2/s. At the patch scale, h_{equil} appears to scale in a similar manner between *Open [std.]* and *Open [EKE]*, as given by γ_{std} and γ_{EKE} discussed above. The qualitative view of the mixed patch development also shows largely comparable patterns between the two, albeit with slightly deeper mixing in *Open [EKE]*. The surface salinity of the mixed patch in *Open [EKE]* is found to stabilize at a slightly lower value compared to *Open [std.]*, which seems to be due to more effective mixing of salinity away from the mixed patch-surface in the former case. However, the resulting difference in $\mathscr{B}_0$ over the mixed patch is negligible in the large-scale.

For the large-scale AMOC adjustment, the adjustment timescales differ slightly but are similar. The absolute values of the AMOC adjustment differ, with stronger adjustment in the case of *Open [EKE]*. This corresponds to a stronger

surface buoyancy flux over the area, and the cause for the stronger surface buoyancy flux has not been isolated. However, when adjusting for the difference in strength of *Ctrl [std.] & Ctrl [EKE]*, the difference is negligible.

The signal propagation along the northern boundary differs slightly between the two, where *Open [std.]* exhibits seemingly constant propagation velocity towards the western boundary, while the signal of *Open [EKE]* appears to propagate at two different velocities, first faster than *std.* and then slower as the western boundary is approached. This could be a matter of differences in slope in the isopycnals between the two configurations, and the final arrival time is similar. Finally, when compared in terms of the Walin-framework, *Open [EKE]* shows diapycnal mixing anomalies and MOC adjustment over a slightly larger range of potential density-layers, but this result does not seem robust enough to draw any conclusions with certainty.

To summarize, the prognostic EKE closure was implemented with the hopes of better representing spatial and temporal variations in meso-scale eddy transfer between the mixed patch and its surroundings, but even though it lead to slight differences at the local scale, the large-scale long-term consequences are seemingly negligible.

5.1.4 Third research question

How do signals propagate from the mixed patch and to the equator in the experiments at hand, and how does the propagation timescales correspond to timescales of MOC adjustment? The initial response of the MOC in each configuration is communicated too fast to be explained by advection in the western boundary, leaving boundary waves as the likely explanation. The signals initially propagate along the northern boundary, with velocities ranging from $\sim 1-4$ cm/s. For the configuration with lateral viscosity $A_h = 5 \times 10^2$ m^2/s, rapid boundary waves along the western boundary can be observed, propagating with Kelvin-like velocities of ~ 1.5 m/s. Boundary waves with velocities like these can not be found in the standard configuration with $A_h = 5 \times 10^4$ m^2/s, likely because the increased viscosity dampens them out. Here, signals with velocities around 9 cm/s are found instead, which is too fast to be explained by advection in the WBC. This suggests that also these signals are communicated by some form of boundary wave. Whether they are Kelvin waves slowed down due to specifics of the model, or short Rossby waves as suggested by Marshall and Johnson (2013) is outside the scope of this thesis to determine. The velocities of these boundary waves largely agree

with the timescales of the initial AMOC adjustment, leading to the conclusion that boundary waves are the likely explanation. However, the timescales of the adjustment towards the steady-state of the MOC seem to correspond better with the slower, stronger signals that are found propagating at ~ 2 cm/s, crossing the northern hemisphere at decadal timescales. These velocities are comparable to meridional velocities in the WBC, and may therefore be advective signals. This suggests that while the initial response is communicated by boundary waves, the adjustment towards steady state may be governed by advection.

5.1.5 Fourth research question

How is upwelling distributed between the WBC and the interior in the model at hand, and how is this affected by the horizontal resolution? For the coarse-resolution model, the same pattern of very strong upwelling in the westernmost grid cells that was pointed out by Huck *et al.* (1999) appears, along with compensating downwelling in the neighbour grid cells. This stands in stark contrast to the classical picture of uniform upwelling of the Stommel-Arons model. The observed pattern persists when considering the upwelling across the approximately corresponding isopycnal layer, although the magnitude of the upwelling is reduced, suggesting that some of the upwelling is along sloping isopycnals in the WBC rather than diapycnal. The upwelling in the WBC is strongly reduced in the $1/6^\circ$ configuration, while still enhanced compared to the rest of the interior. If the excessive upwelling seen in coarse-resolution models is a consequence of coarse-resolution boundary layer dynamics, as suggested by Huck *et al.* (1999), the weaker upwelling in the $1/6^\circ$ model may be explained by better resolved boundary layers. These results emphasize the importance of further research on what governs the upwelling at the WBC, and how this enhanced upwelling impacts the AMOC as a whole. As the upwelling branch is slightly outside of the scope of this thesis, further discussion on upwelling will not be attempted here.

5.2 Limitations and further research

With more time, a natural way forward would be to ensure reliable long-term experiments in the $1/6^\circ$ configuration. Due partly to the importance of mesoscale eddy transport in setting the properties of the mixed patch, partly to the expectation that boundary wave velocities may be dependent on resolution, and partly to the evident dependency on model resolution in WBC upwelling,

it would be interesting to see how the AMOC adjusts to open-ocean convection in an eddy-permitting model. It is unfortunate that, despite many attempts, this was not achieved in the present work.

As discussed in section 2.2, a key property of open-ocean convection is that it is constrained in space and *time*. Only the former is true for the experiments conducted here. Once experiments are initiated, the additional surface salinity forcing is kept on for the remainder of the run time, although gradually declining in strength as the local surface salinity approaches S_f. Buckley *et al.* (2023) suggests that frequency of the variation in surface buoyancy forcing is important, where high-frequency variation (seasonal or shorter) changes the deep convection and the NADW formation, but has less of an impact on NADW export to the subtropics, while low-frequency variations result in changes to the exported water masses. It would be interesting to test the consequences of adding a periodically varying signal, for example with seasonal peaks, and see if the same can be found here.

As was briefly mentioned in section 4.3, the densest water masses formed during the experiments do not share any isopycnals out of the northern region at the time they are formed. This is not necessarily the case in real open-ocean convection, and may impact how the newly formed water masses spread from the forcing region. A longer spin-up time, so that dense water has sufficiently spread across the abyss before the experiments are initiated, may improve this.

Finally, all experiments have been conducted in a highly idealized model basin. It is expected that more complex bottom topology, sloping vertical boundaries, surface wind stress and more complex basin geometries may impact the processes at hand. One aspect to note in particular is that open-ocean convection is often observed in marginal seas such as the Labrador Sea, with unique dynamics related to inflow, outflow and boundary currents. This is expected to play a role in the export of dense water formed by convection, and by extension the connection between convective regions and the AMOC (Marshall and Schott, 1999; Johnson *et al.*, 2019). Investigating open-ocean convection in more complex model configurations is therefore essential in the process of understanding its full role in the global circulation, and possible role in transient behaviour of the AMOC.

Bibliography

6

Andreasen, Laurits S. (2019). “Time scales of the Bipolar seesaw: The role of oceanic cross-hemisphere signals, Southern Ocean eddies and wind changes”. MA thesis. University of Copenhagen.

Brüggemann, Nils and Caroline A. Katsman (2019). “Dynamics of Downwelling in an Eddying Marginal Sea: Contrasting the Eulerian and the Isopycnal Perspective”. *Journal of Physical Oceanography* 49.11, pp. 3017–3035.

Buckley, Martha W., David Ferreira, Jean-Michel Campin, John Marshall, and Ross Tulloch (2012). “On the Relationship between Decadal Buoyancy Anomalies and Variability of the Atlantic Meridional Overturning Circulation”. *Journal of Climate* 25.23, pp. 8009–8030.

Buckley, Martha W., M. Susan Lozier, Damien Desbruyères, and Dafydd Gwyn Evans (2023). “Buoyancy forcing and the subpolar Atlantic meridional overturning circulation”. *Philosophical Transactions of the Royal Society A: Mathematical, Physical and Engineering Sciences* 381.2262, p. 20220181.

Buckley, Martha W. and John Marshall (Mar. 2016). “Observations, inferences, and mechanisms of the Atlantic Meridional Overturning Circulation: A review”. *Reviews of Geophysics* 54.1, pp. 5–63.

Chelton, Dudley B., Roland A. deSzoeke, Michael G. Schlax, Karim El Naggar, and Nicolas Siwertz (1998). “Geographical Variability of the First Baroclinic Rossby Radius of Deformation”. *Journal of Physical Oceanography* 28.3, pp. 433–460.

Courtois, Peggy, Xianmin Hu, Clark Pennelly, Paul Spence, and Paul G. Myers (Dec. 2017). “Mixed layer depth calculation in deep convection regions in ocean numerical models”. *Ocean Modelling* 120, pp. 60–78.

Eden, C. (2014). *pyOM2.0 Documentation*. `https://veros.readthedocs.io/en/latest/introduction/introduction.html`. Frozen documentation that VEROS is based on, accessed: 19.03.2024.

Eden, Carsten and Richard J. Greatbatch (Jan. 2008). “Towards a mesoscale eddy closure”. *Ocean Modelling* 20.3, pp. 223–239.

Gaspar, Philippe, Yves Grégoris, and Jean-Michel Lefevre (1990). “A simple eddy kinetic energy model for simulations of the oceanic vertical mixing: Tests at station Papa and long-term upper ocean study site”. *Journal of Geophysical Research: Oceans* 95.C9, pp. 16179–16193.

Gent, P. R., J. Willebrand, T. J. McDougall, and J. C. McWilliams (1995). “Parameterizing Eddy-Induced Tracer Transports in Ocean Circulation Models”. *Journal of Physical Oceanography* 25, pp. 463–474.

Gent, Peter R and James C Mcwilliams (1990). “Isopycnal mixing in ocean circulation models”. *Journal of Physical Oceanography* 20.1, pp. 150–155.

Getzlaff, J., C. W. Böning, C. Eden, and A. Biastoch (2005). “Signal propagation related to the North Atlantic overturning”. *Geophysical Research Letters* 32.9, 2004GL021002.

Green, JSA (1970). “Transfer properties of the large-scale eddies and the general circulation of the atmosphere”. *Quarterly Journal of the Royal Meteorological Society* 96.408, pp. 157–185.

Griffies, Stephen M. (1998). “The Gent–McWilliams Skew Flux”. *Journal of Physical Oceanography* 28.5, pp. 831–841.

Häfner, Dion, René Løwe Jacobsen, Carsten Eden, Mads R. B. Kristensen, Markus Jochum, Roman Nuterman, and Brian Vinter (2018). “Veros v0.1 – a fast and versatile ocean simulator in pure Python”. *Geoscientific Model Development* 11.8, pp. 3299–3312.

Hansen, Rasmus R. (2023). “Solving the turbulence closure problem II”. MA thesis. University of Copenhagen.

Huck, Thierry, Andrew J Weaver, and Alain Colin de Verdière (1999). “On the influence of the parameterization of lateral boundary layers on the thermohaline circulation in coarse-resolution ocean models”. *Journal of marine research* 57.3, pp. 387–426.

Ilıcak, Mehmet, Alistair J. Adcroft, and Sonya Legg (2014). “A framework for parameterization of heterogeneous ocean convection”. *Ocean Modelling* 82, pp. 1–14.

Johnson, Helen L., Paola Cessi, David P. Marshall, Fabian Schloesser, and Michael A. Spall (2019). “Recent Contributions of Theory to Our Understanding of the Atlantic Meridional Overturning Circulation”. *Journal of Geophysical Research: Oceans* 124.8, pp. 5376–5399.

Jones, H. and J. Marshall (1993). “Convection with Rotation in a Neutral Ocean: A Study of Open-Ocean Deep Convection”. *Journal of Physical Oceanogr.* 23, pp. 1009–1039.

Kawase, M. (1987). “Establishment of Deep Ocean Circulation Driven by Deep-Water Production”. *Journal of Physical Oceanography* 17, pp. 2294–2317.

Klinger, Barry A., John Marshall, and Uwe Send (1996). “Representation of convective plumes by vertical adjustment”. *Journal of Geophysical Research: Oceans* 101.C8, pp. 18175–18182.

Kovalevsky, Dmitry V., Igor L. Bashmachnikov, and Genrikh V. Alekseev (2020). “Formation and decay of a deep convective chimney”. *Ocean Modelling* 148, p. 101583.

Kuhlbrodt, T., A. Griesel, M. Montoya, A. Levermann, M. Hofmann, and S. Rahmstorf (2007). “On the driving processes of the Atlantic meridional overturning circulation”. *Reviews of Geophysics* 45.2, 2004RG000166.

Li, F., M. S. Lozier, S. Bacon, *et al.* (2021). “Subpolar North Atlantic western boundary density anomalies and the Meridional Overturning Circulation”. *Nature Communications* 12.1, p. 3002.

Marotzke, Jochem (2023). “From theory to RAPID AMOC observations: a personal voyage of discovery”. *Philosophical Transactions of the Royal Society A: Mathematical, Physical and Engineering Sciences* 381.20220192.

Marotzke, Jochem and Barry A. Klinger (May 2000). “The Dynamics of Equatorially Asymmetric Thermohaline Circulations”. *Journal of Physical Oceanography* 30.5, pp. 955–970.

Marshall, David P. and Helen L. Johnson (2013). “Propagation of Meridional Circulation Anomalies along Western and Eastern Boundaries”. *Journal of Physical Oceanography* 43.12, pp. 2699–2717.

Marshall, J., A. Whitehead, and T. Yates (1994). “Laboratory and numerical experiments in ocean convection”. *Ocean Processes in Climate Dynamics: Global and Mediterranean Examples*. Ed. by P. Malanotte-Rizzoli and A. R. Robinson. Dordrecht: Springer Science+Business Media. Chap. 8, pp. 173–201.

Marshall, John and Friedrich Schott (1999). “Open-ocean convection: Observations, theory, and models”. *Reviews of Geophysics* 37.1, pp. 1–64.

Maxworthy, T and S Narimousa (1994). “Unsteady, turbulent convection into a homogeneous, rotating fluid, with oceanographic applications”. *Journal of Physical Oceanography* 24.5, pp. 865–887.

Pedlosky, Joseph (1996). *Ocean circulation theory*. Springer Science & Business Media.

Reverdin, G., E. Kestenare, C. Frankignoul, and T. Delcroix (2007). “Surface salinity in the Atlantic Ocean (30°S–50°N)”. *Progress in Oceanography* 73.3–4, pp. 311–340.

Send, Uwe and John Marshall (1995). “Integral effects of deep convection”. *Journal of physical oceanography* 25.5, pp. 855–872.

Sohail, Taimoor, Bishakhdatta Gayen, and Andrew McC. Hogg (2020). “The Dynamics of Mixed Layer Deepening during Open-Ocean Convection”. *Journal of Physical Oceanography* 50.6, pp. 1625–1641.

Spall, Michael A. and Robert S. Pickart (2001). “Where Does Dense Water Sink? A Subpolar Gyre Example”. *Journal of Physical Oceanography* 31.3, pp. 810–826.

Stöber, Uwe, Maren Walter, Christian Mertens, and Monika Rhein (2008). “Mixing estimates from hydrographic measurements in the deep western boundary current of the North Atlantic”. *Deep Sea Research Part I: Oceanographic Research Papers* 55.6, pp. 721–736.

Stone, Peter H (1972). “A simplified radiative-dynamical model for the static stability of rotating atmospheres”. *Journal of the Atmospheric Sciences* 29.3, pp. 405–418.

Vallis, Geoffrey K (2017). *Atmospheric and Oceanic Fluid Dynamics*. 2nd. Cambridge University Press.

Visbeck, Martin, John Marshall, and Helen Jones (1996). “Dynamics of isolated convective regions in the ocean”. *Journal of Physical Oceanography* 26.9, pp. 1721–1734.

Walin, Gösta (1982). “On the relation between sea-surface heat flow and thermal circulation in the ocean”. *Tellus* 34.2, pp. 187–195.

Weaver, Andrew J and ES Sarachik (1990). “On the importance of vertical resolution in certain ocean general circulation models”. *Journal of Physical Oceanography* 20.4, pp. 600–609.

Xu, Xiaobiao, Peter B. Rhines, and Eric P. Chassignet (Oct. 2018). “On Mapping the Diapycnal Water Mass Transformation of the Upper North Atlantic Ocean”. *Journal of Physical Oceanography* 48.10, pp. 2233–2258.

Zhang, Rong (Aug. 2010). “Latitudinal dependence of Atlantic meridional overturning circulation (AMOC) variations”. *Geophysical Research Letters* 37.16, 2010GL044474.

Appendix

A

A.1 Attempted high-resolution configurations

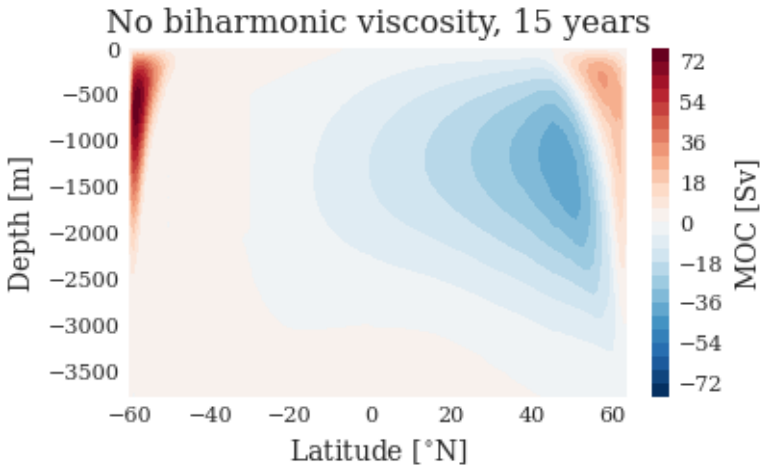

Figure A.1.: Overturning ciruclation in high-resolution configuration identical to standard *HR*, except with no biharmonic viscosity

Here, I show the two main challenges that riddled my eddy-permitting model set-up. First is the results of a configuration identical to the one described in Chapter 3, except with no biharmonic viscosity. Here, as can be seen in Figure A.1, grid-scale noise dominates near the northern and southern boundaries, leading to spurious upwelling in the north. The grid-scale noise was persistent despite attempts at varying either lateral viscosity A_h or diffusivities K_{iso} and K_{gm} (not shown here).

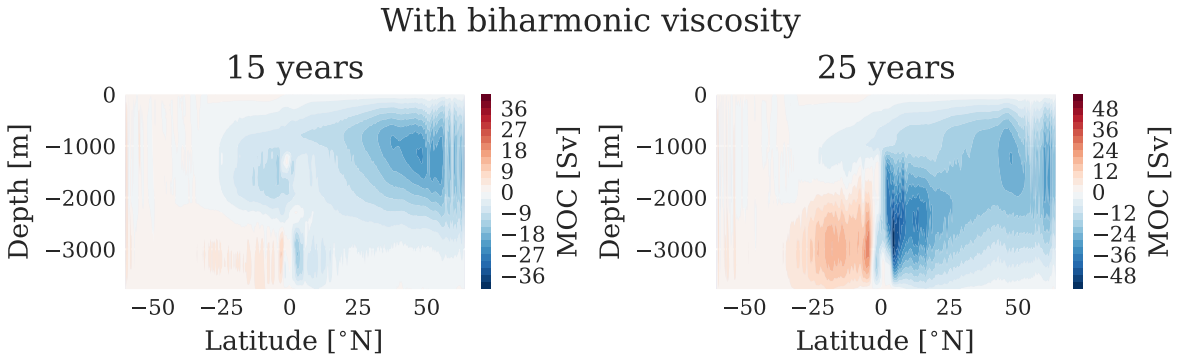

Figure A.2.: Overturning circulation in *HR*-configuration used in the experiments of the thesis, at 15 years and 25 years.

The only tested adjustment that removed the dominating grid-scale noise near the boundaries, was including biharmonic viscosity A_{hbi}. This, however, brought on a new problem, namely a pattern of instability at depths near the equator. This eventually developed to completely dominate the overturning circulation, which never reached steady-state but kept on strengthening over time. Figure A.2 shows the pattern already developing after 15 years, but at this times the northern cell is still looking somewhat as expected. After 25 years however, the cell seems to completely dominated by what is happening near the equator. Unfortunately, there was no time to investigate the cause nor the solution to this problem. However, it seems similar to the problem described in Weaver and Sarachik (1990), where it was found that increasing the vertical resolution solved the problem. Such an approach will be an appropriate starting point for further research.